Mon. Not. R. Astron. Soc. **000**, 1–20 (2011) Printed 17 January 2021 (MN LATEX style file v2.2)

Black hole mass estimate for a sample of radio–loud Narrow–line Seyfert 1 galaxies

G. Calderone[1⋆], G. Ghisellini[2], M. Colpi[1,3], M. Dotti[1,3]
[1] *Università di Milano - Bicocca, Dip. di Fisica G. Occhialini, Piazza della Scienza 3, I-20126 Milano, Italy*
[2] *INAF Osservatorio Astronomico di Brera, Via E. Bianchi 46, I-23807 Merate (LC), Italy*
[3] *INFN Sezione Università di Milano - Bicocca, Piazza della Scienza 3, I-20126 Milano, Italy*

17 January 2021

ABSTRACT
We discuss the relationship between a standard Shakura & Sunyaev (1973) accretion disk model and the Big Blue Bump (BBB) observed in Type 1 AGN, and propose a new method to estimate black hole masses. We apply this method to a sample of 23 radio–loud Narrow–line Seyfert 1 (RL–NLS1) galaxies, using data from WISE (Wide-field Infrared Survey Explorer), SDSS (Sloan Digital Sky Survey) and GALEX. Our black hole mass estimates are at least a factor ∼6 above previous results based on single epoch virial methods, while the Eddington ratios are correspondingly lower. Hence, the black hole masses of RL–NLS1 galaxies are typically above $10^8 M_\odot$, in agreement with the typical black hole mass of blazars.

Key words: accretion discs, galaxies: jets, quasars: emission lines

1 INTRODUCTION

The Spectral Energy Distribution (SED) of Active Galactic Nuclei (AGN) spans several orders of magnitude in frequency and results from the superposition of radiation emitted by different components.

In radio–quiet Type 1 sources, characterized by the presence of broad emission lines in their optical spectrum, the most luminous components are the "Big Blue Bump" (BBB, between ∼1 μm and ∼3 nm, or $\log(\nu/\mathrm{Hz})$ ∼14.5–17) and the "infrared bump" (IR bump, between ∼1 mm and ∼1 μm or $\log(\nu/\mathrm{Hz})$ ∼11.5–14.5). The former is the most prominent feature in the SED (Sanders et al. 1989; Elvis et al. 1994; Richards et al. 2006), while the latter accounts for 20–40% of the bolometric AGN luminosity. The BBB is thought to be thermal radiation from the accretion disk, while the IR bump is thermal radiation emitted from a dusty torus located a ∼1 pc from the black hole (Sanders et al. 1989). Superimposed to the BBB there is often a minor component named "Small Blue Bump" (SBB, extending from 2200Å to 4000Å) which is likely the blending of several iron lines and hydrogen Balmer continuum (Wills et al. 1985; Vanden Berk et al. 2001). This scheme roughly describes the SED of AGN over at least 5 orders of magnitude in bolometric luminosity (Sanders et al. 1989; Elvis et al. 1994; Richards et al. 2006). It also applies to powerful blazars, although in these cases two more components are needed to describe the entire SED: the "synchrotron hump" (extending from radio to IR/optical wavelengths) and the "Compton hump" (extending from X–rays to TeV energies) which may overwhelm the torus and the BBB radiation. These further components characterize radio–loud sources whose jet is closely aligned to the line of sight, and are due to the synchrotron and inverse Compton processes, respectively.

The common energy production process in AGN is believed to be accretion onto a super–massive black hole ($M \sim 10^{6-10} M_\odot$), through a disk whose observational properties depend (among other parameters) on the black hole mass and accretion rate. This interpretation led several authors to use models of geometrically thin, optically thick accretion disks (Shakura & Sunyaev 1973, hereafter AD model) to fit the optical/UV SED of AGN in order to determine the black hole mass and the accretion rate (e.g. Shields 1978; Malkan & Sargent 1982; Malkan 1983; Zheng et al. 1995; Sun & Malkan 1989). The AD fitting method allowed to estimate such quantities for those active nuclei which are too distant ($z \gtrsim 0.1$) or too bright for other direct methods, such as resolved stellar/gas dynamics, to be applied (Ferrarese & Ford 2005). However, as discussed extensively in Koratkar & Blaes (1999) and references therein, such simple models provide only rough fits to the observed data. Among the major issues with this interpretation, we point out a few ones: the broad–band continuum slopes α_ν (with $F_\nu \propto \nu^{\alpha_\nu}$) at optical–NUV wavelengths found in literature (e.g. Neugebauer et al. 1979; Vanden Berk et al. 2001;

⋆ E-mail: giorgio.calderone@mib.infn.it

Davis et al. 2007; Bonning et al. 2007) are incompatible with the slope $\alpha_\nu = 1/3$, expected from the AD model; the spectrum from a simple accretion disk does not reproduce the observed power law extending at X–rays and the soft X–ray excess (e.g. Pounds et al. 1986; Nandra & Pounds 1994; Fabian & Miniutti 2005); the gross properties of the spectrum of radio–quiet AGN appear to scale with the luminosity (Sanders et al. 1989; Walter & Fink 1993), but does not shift in frequency (Laor & Davis 2011a). The latter issue indicates that the BBB spectrum peaks always at, or near, the same frequency. However, this observation is hard to reconcile with reasonably broad distributions of black hole masses, accretion rates, inclinations and radiative efficiencies. Given these difficulties, the AD fitting method is not widely employed as a black hole mass estimation method. Rather, it is sometimes used to indirectly infer other parameters such as the accretion efficiency (Davis & Laor 2011; Laor & Davis 2011a, but see Raimundo et al. 2012) or to explain specific quasar properties (Laor & Davis 2011b), while the black hole mass is usually estimated using reverberation mapping calibrated scaling relations (the so–called "single epoch virial method", or SE virial, Peterson 1993; Peterson et al. 2004; Onken et al. 2004; Vestergaard & Peterson 2006; Bentz et al. 2009).

The SE virial method is currently employed to estimate black hole masses in large catalogs (e.g. Shen et al. 2011) for its simple applicability. However, the resulting black hole mass estimates are known to be affected by uncertainties of a factor of $\sim$3 (Park et al. 2012). In addition, there may be systematic uncertainties related to the Broad Line Region (BLR) geometry and inclination; the role of radiation pressure; the modeling of emission line profiles; the contribution from other components (e.g. host galaxy); intrinsic differences between different AGN; and whether gravity dominates the motions of the BLR clouds (Krolik 2001; Marconi et al. 2008; Decarli et al. 2008, 2011; Peterson 2011). Black hole masses estimated in this way are subjected to a number of assumptions and may therefore be just order of magnitude estimates (e.g. Croom 2011, but see Assef et al. 2012).

There has been claims about the existence of a correlation between the SE virial mass and the radio luminosity, either absolute (Franceschini et al. 1998) or normalized to the optical luminosity (i.e. the radio loudness parameter, Laor 2000). It was further noticed that a black hole mass greater than $\sim 3 \times 10^8 M_\odot$ would be required in order to develop a relativistic jet as observed in powerful blazars. Later, these findings have been revisited with the availability of larger samples. Woo & Urry (2002) found that both the radio–quiet and radio–loud AGN span the same range of black hole mass, and that there is no evidence for a strong correlation between the radio–loudness and black hole mass. Recently, the issue on the black hole mass threshold has been revisited by Chiaberge & Marconi (2011): by taking into account the radiation pressure on the BLR clouds in computing the SE virial masses they found that a black hole mass $\gtrsim 10^8$ is required to produce a radio–loud AGN.

In this paper we revisit the AD spectrum fitting method and show (§2) that the AD model provides a rather satisfactory description of the Type 1 AGN SED in the majority of cases (at least at optical/NUV wavelengths) once the contributions from other emitting components (such as host galaxy and/or jet) have been properly taken into account. Therefore, the AD modeling method is a viable and independent way to estimate black hole masses. This is particularly interesting for a class of AGN sources for which black hole masses are suspected to be systematically underestimated by the SE virial method: the Narrow Line Seyfert 1 (NLS1) galaxies (Marconi et al. 2008; Decarli et al. 2008; Peterson 2011).

NLS1 sources are characterized by the relatively small values of the full width at half maximum (FWHM) of the "broad" component of the Hβ emission line (FWHM(Hβ) $<$ 2000 km s^{-1}), by the presence of strong blended iron lines, and of a prominent soft X–ray excess (Osterbrock & Pogge 1985; Pogge 2000). By estimating the virial black hole mass using the Hβ emission line, and [O III] width as a surrogate for the bulge stellar velocity dispersion, Grupe & Mathur (2004) and (Mathur & Grupe 2005) claimed that NLS1 lie systematically below the M–σ_* of non–active and active Broad Line galaxies (BLS1). This indicates that the black hole masses of NLS1 are systematically smaller than the black hole masses of BLS1 for a given value of σ_*. The same considerations apply when considering objects of the same luminosity: NLS1 appear to accrete at a higher Eddington ratio with respect to BLS1, with some objects exceeding the Eddington luminosity (Zhou et al. 2006).

Recently, a few NLS1 sources have been confirmed to be part of a new class of γ–ray emitting sources, as detected by *Fermi*/LAT (Abdo et al. 2009a,c; Foschini 2011), besides blazars and radio–galaxies. Variability of the γ–ray emission (Calderone et al. 2011) allows to exclude a starburst origin of the γ–rays and confirms the presence of powerful relativistic jets, such as those found in typical blazars. The emerging picture is that γ–NLS1 sources are very similar to powerful blazars, except for their small widths of broad lines, and consequently their small SE virial black hole masses ($10^{6-8} M_\odot$, Yuan et al. 2008). Hence these sources are the best candidates to settle the question on whether very massive black holes ($\gtrsim 10^8 M_\odot$) power relativistic jets. If the SE virial mass estimates will be confirmed this would imply that a large mass is not required to produce a radio–loud AGN. On the other hand, if masses turn out to be systematically under–estimated in NLS1, we would then conclude that extragalactic jetted sources preferentially live in large black hole mass systems.

Furthermore we may find that NLS1 too lie on the "canonical" M–σ_* relation of broad line sources and accrete close to (albeit below) the Eddington rate. Possible explanations for the observed small widths of the broad lines in NLS1 include: the virial mass scaling relations may need to be modified in order to account for radiation pressure effects (Marconi et al. 2008; Chiaberge & Marconi 2011); the BLR may have a disk–like geometry and be oriented almost face-on, so that the Doppler shifted line velocity, projected along the line of sight, turns out to be small (Decarli et al. 2008); a combination of these effects (Peterson 2011).

In this work we show that the broad–band composite SEDs of AGN are roughly compatible with a simple, non–relativistic AD model (§2), and discuss a method to estimate the total disk luminosity using either the continuum (§2.1) or the line luminosities (§2.2) as proxy. Then, we perform a spectroscopic analysis of the SDSS spectra of 23 radio–loud NLS1 (§3) in order to disentangle the host galaxy and/or jet

contribution from the AGN continuum, and estimate line luminosities (§3.1). In §4 we discuss a new method to estimate the black hole mass and accretion rate, using AD spectrum modeling, and apply this method on the afore mentioned sample. We discuss our results in §5 and 6, and draw our conclusion in §7. The observational properties of the Shakura & Sunyaev (1973) AD model are summarized in the appendix.

Throughout the paper, we assume a ΛCDM cosmology with $H_0 = 71$ km s^{-1} Mpc^{-1}, $\Omega_m = 0.27$, $\Omega_\Lambda = 0.73$.

1.1 Notation

In what follows we will consider a non–relativistic,[1] steady state, geometrically thin, optically thick accretion disk (Shakura & Sunyaev 1973), extending from $R_{in} = 6R_g$ to $R_{out} = 2 \times 10^3 R_g$, where $R_g = GM/c^2$ is the gravitational radius of the black hole. The integrated disk luminosity is $L_d = \int L_\nu d\nu = \eta \dot{M} c^2$, with $\eta \sim 0.1$ (radiative efficiency). The corresponding Eddington ratio is $\ell = L_d/L_{Edd}$ with $L_{Edd} = 1.3 \times 10^{47} (M/10^9 M_\odot)$ erg s^{-1}.

The relation between the disk luminosity and its "isotropic equivalent" counterpart is $L_d^{iso} = \langle 2\cos\theta \rangle L_d$ (Eq. A13), where θ is the angle between the normal to the disk and the line of sight. For Type 1 AGN we take $\langle 2\cos\theta \rangle = 1.7$ (Eq. A16).

We will refer to the peak frequency in the νL_ν representation as ν_p, and to the luminosity of the peak as $\nu_p L_{\nu_p}$. These quantities scale with the physical parameters as follows (Eq. A8 and A9):

$$\nu_p \propto M^{-1/2} \dot{M}^{1/4}$$
$$\nu_p L_{\nu_p} \propto \dot{M}.$$

In particular we notice that $\nu_p L_{\nu_p} \sim 0.5 L_d$ (Eq. A10). The location of the peak (i.e. its luminosity and frequency) determines uniquely the black hole mass and accretion rate. Details about the observational properties of the AD spectrum are given in appendix A1.

All spectral slopes α_ν are defined as $F_\nu \propto \nu^{\alpha_\nu}$.

2 ACCRETION DISK SPECTRUM IN AGN SPECTRA

Richards et al. (2006) built an average Type 1 QSO SED using data from 259 (mainly radio–quiet) sources, observed with instruments ranging from radio wavelengths to X–rays. Individual SEDs have been interpolated between available bands. An average SED is then computed as a geometric mean of individual ones, and is shown in Fig. 1, (red line). Also shown in Fig. 1 are: a spiral galaxy template as given in Mannucci et al. (2001, orange), normalized to have a bolometric luminosity of $10^{45.5}$ erg s^{-1}; the location of the Small Blue Bump (SBB, Wills et al. 1985; Vanden Berk et al. 2001); three reference frequencies corresponding to 5100Å, 3000Å and 1350Å (red filled circles), commonly used in calculation of bolometric luminosity (see below); the average spectral slopes found in literature, as measured on composite spectra at near IR, optical/UV (Vanden Berk et al. 2001, green) and far UV wavelengths (Telfer et al. 2002, purple); the rest frame frequency range covered by SDSS, for values of z =0, 0.3, 1, 2 and 3 (thin blue lines). Finally, we show the AD spectrum that best fits the composite Type 1 SED at optical/UV wavelengths (black line). The parameter for the AD model are: $\log(M/M_\odot)$=9, ℓ=0.05 and $\theta = 30°$.

The agreement between the AD model and the composite SED is rather good, therefore the association between the BBB and thermal emission from simple AD model is justified, at least in the interval 1000–5000Å, or $\log(\nu/\mathrm{Hz})$=14.8–15.5 (black dotted vertical lines). A few discrepancies between the AD model and the composite Type 1 QSO SED arise:

- at $\log(\nu/\mathrm{Hz}) <$14.7 a further component emerges in the spectrum, which may be either the host galaxy, the emission from a dusty torus or some other component;
- at $\log(\nu/\mathrm{Hz}) \sim$15 a Small Blue Bump (SBB) is present, likely due to a blending of iron lines and Hydrogen Balmer continuum;
- at $\log(\nu/\mathrm{Hz}) \gtrsim$15.6 other physical components contribute to the flux (e.g. a corona).

Note that, in this interpretation of the BBB, the portion of the AD spectrum characterized by the $\alpha_\nu = 1/3$ slope (thick blue line) is hidden by the host galaxy and the torus components, and cannot be revealed directly with observations (although in some case it may be detected in polarized light, Kishimoto et al. 2008). The average slopes at optical/UV and far UV (green and purple lines) are roughly consistent with the slopes near the peak of the AD spectrum. We notice however that fixed spectral features (such as the SBB) may affect the estimation of spectral slopes. Furthermore, the value of the slope likely depends on the width of the wavelength range inside which it is defined. Therefore it is not always possible to infer the presence of an AD spectrum by just checking the spectral slopes at optical/UV wavelengths. By contrast, at near IR the average slope (green line) is inconsistent with an AD spectrum, but this is likely due to the host galaxy component.

We conclude that the AD model provides a reasonable description of the gross properties of Type 1 AGN SED at optical/NUV wavelengths, and the similarity between the predicted spectrum and the average BBB is rather strong. Under this assumption it is possible to infer the black hole mass and the accretion rate by comparing the observed SED with the AD spectrum, as discussed in §4. Our black hole mass estimation method requires an estimate of the disk luminosity (L_d), as discussed in the following two sections.

2.1 Continuum luminosity as a proxy to disk luminosity

The broad–band similarity among AGN spectra allows to use the continuum luminosity at a given wavelength as a proxy for the bolometric luminosity, that is $L_{bol} = C_{bol} \times \lambda L_\lambda$. In order to explore this relationship Richards et al. (2006) measured the bolometric luminosity for each spectrum (defined to be the integral isotropic luminosity between 100μm and 10 keV) and derived a bolometric correction (C_{bol}) based on the continuum luminosity at 3000Å, 5100Å

[1] General relativistic correction are negligible for the purpose of our work, see §A4

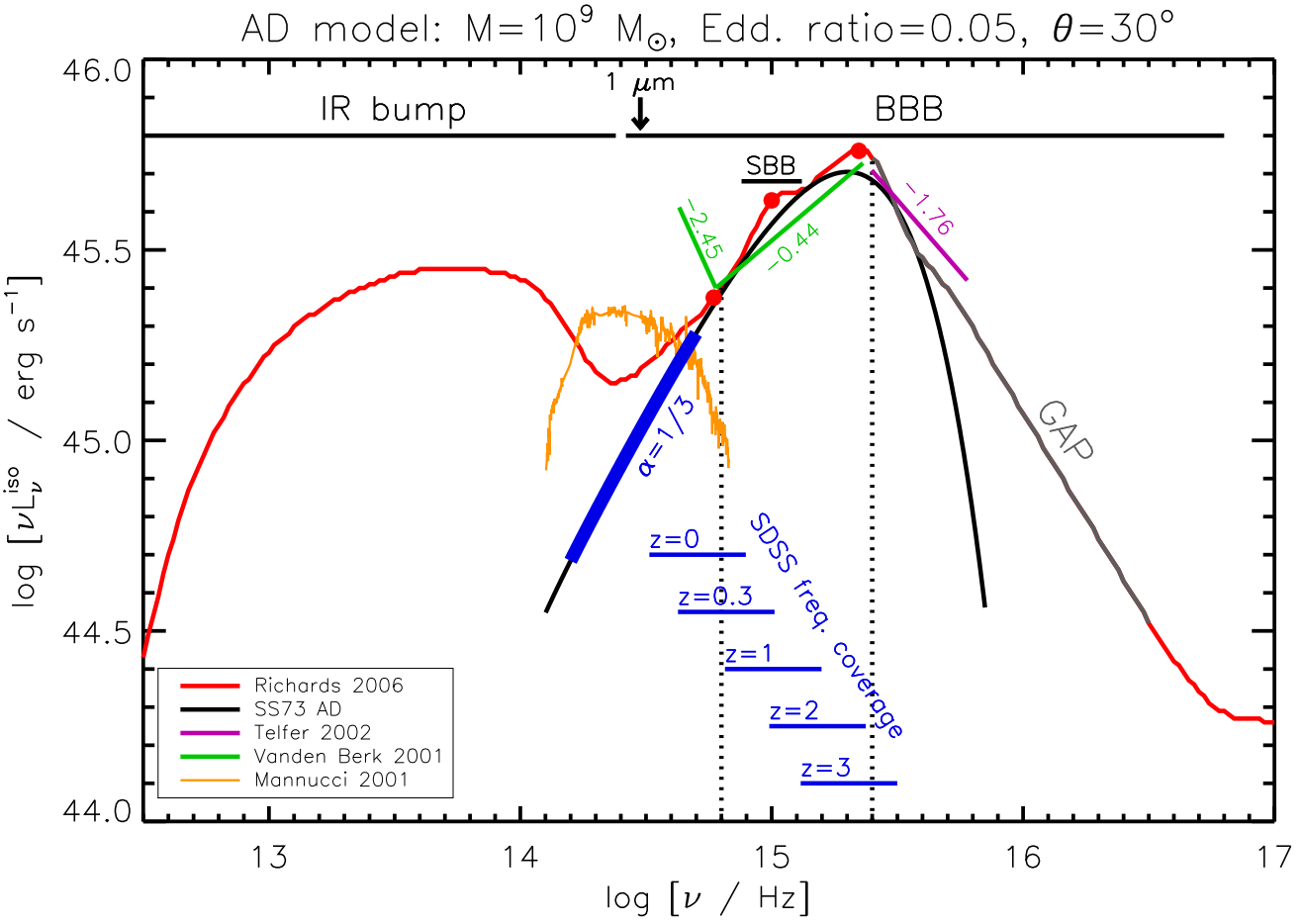

Figure 1. Comparison of the composite Type 1 AGN SED (red line) from Richards et al. (2006) and an AD model (§1.1) for $\log(M/M_{\odot})$=9, ℓ=0.05 and $\theta = 30°$ (black line). Also shown are: a spiral galaxy template as given in Mannucci et al. (2001, orange), normalized to have a bolometric luminosity of $10^{45.5}$ erg s^{-1}; the location of the Small Blue Bump (SBB, Wills et al. 1985; Vanden Berk et al. 2001); three reference frequencies corresponding to 5100Å, 3000Å and 1350Å (red filled circles), commonly used in calculation of bolometric luminosity; the average spectral slopes found in literature, as measured on composite spectra at near IR, optical/UV (Vanden Berk et al. 2001, green) and far UV wavelengths (Telfer et al. 2002, purple); the rest frame frequency range covered by SDSS, for values of z =0, 0.3, 1, 2 and 3 (thin blue lines). Thick blue line highlights the portion of the AD spectrum characterized by the slope $\alpha_{\nu} = 1/3$. The rest frame frequency range inside which the AD model reproduces the shape of the AGN composite SED ($\log(\nu/\mathrm{Hz})$=14.8–15.5) is shown with dotted black lines.

and 3μm. The resulting values are: $C_{\rm bol}(3000\text{Å}) = 5.62 \pm 1.14$, $C_{\rm bol}(5100\text{Å}) = 10.33 \pm 2.08$, $C_{\rm bol}(3\mu\mathrm{m}) = 9.12 \pm 2.62$. The distribution of $C_{\rm bol}$ values is relatively narrow, with a relative dispersion of the order of ∼20%. Note however, that in particular cases the $C_{\rm bol}$ value can differ by as much as 50% from the mean value. Shen et al. (2011, hereafter S11 catalog) have slightly re–calibrated the $C_{\rm bol}$ values, and extended the analysis to 1350Å, in order to compute bolometric luminosities for all the sources in their sample. Their values are: $C_{\rm bol}(5100\text{Å}) = 9.26$, $C_{\rm bol}(3000\text{Å}) = 5.15$ and $C_{\rm bol}(1350\text{Å}) = 3.81$.

In order to calibrate analogous relations to estimate the disk luminosity $L_{\rm d}^{\rm iso}$ we numerically estimate the bolometric luminosity of the composite SED in Richards et al. (2006), and compare it with the disk luminosity for the AD model shown in Fig. 1. The resulting relation is:

$$L_{\rm d}^{\rm iso} \sim \frac{1}{2} L_{\rm bol} \qquad (1)$$

Then, we compare $L_{\rm d}^{\rm iso}$ with the luminosities at 5100Å, 3000Å and 1350Å wavelengths, as measured on the composite SED:

$$\begin{aligned} L_{\rm d}^{\rm iso} &\sim 4.4\ \nu L_{\nu}(5100\text{Å}) \\ L_{\rm d}^{\rm iso} &\sim 2.4\ \nu L_{\nu}(3000\text{Å}) \\ L_{\rm d}^{\rm iso} &\sim 1.8\ \nu L_{\nu}(1350\text{Å}) \end{aligned} \qquad (2)$$

The locations of these wavelengths are shown with red filled circles in Fig. 1. Considering the uncertainties (∼20%) of $C_{\rm bol}$ we conclude that our relations (Eq. 1 and 2) are compatible with those of S11. Eq. 2 provides a reliable estimate of $L_{\rm d}^{\rm iso}$ as long as the source continuum is not dominated by other emitting components such as host galaxy starlight or synchrotron radiation from a relativistic jet (for radio–loud sources). In these cases we need alternative luminosity estimators, as discussed in the following section.

2.2 Line luminosities as a proxy to disk luminosity

Relations similar to Eq. 2 can be obtained by using line luminosities. Line ratios are known to be approximately constant among AGN (Francis et al. 1991; Vanden Berk et al. 2001): by setting the Lyα luminosity to 100, relative luminosities of Hβ, Mg II and C IV (both narrow and broad components) lines are 22, 34 and 63, respectively, while the total line luminosity is 555.8 (Francis et al. 1991; Celotti et al. 1997). Therefore it is possible to have a rough estimate of the luminosity of all emission lines by measuring the luminosity of a single line. Also, according to the photo–ionization model, the line–emitting gas is ionized by the accretion disk continuum radiation. Therefore we expect (to a first approximation) the disk to line luminosity ratio to be a constant: $L_{\rm d}^{\rm iso} = \kappa\, L_{\rm line}$. This provides a way to estimate the disk luminosity using a single (or a few) line luminosity estimates. In order to calibrate the κ parameter we consider all sources in the S11 catalog having both a continuum and line luminosity estimate for at least one of the combinations: 5100Å–Hβ, 3000Å–Mg II and 1350Å–C IV. The number of sources in each subsample are 22644, 85514 and 52157 respectively (note that a single source typically belongs to two such subsamples). For each source we estimate $L_{\rm line}$ using the broad and narrow line luminosities given in S11 and the coefficients given in Francis et al. (1991) and Celotti et al. (1997). Then we compute the κ parameter as follows:

$$\kappa = \frac{L_{\rm d}^{\rm iso}({\rm Eq.2})}{L_{\rm line}} \qquad (3)$$

where the disk luminosity $L_{\rm d}^{\rm iso}$ is computed using the continuum luminosity given in S11, and Eq. 2. The distributions of κ for the three combinations are approximately log–normal (Fig. 2, upper panel) with median values:

$$\begin{aligned} &\log\kappa(5100\text{Å} - {\rm H}\beta) = 1.08 \pm 0.28 \\ &\log\kappa(3000\text{Å} - {\rm Mg\,II}) = 1.10 \pm 0.21 \\ &\log\kappa(1350\text{Å} - {\rm C\,IV}) = 0.92 \pm 0.28 \end{aligned} \qquad (4)$$

The widths of the κ distributions in Fig. 2 show that the disk luminosity $L_{\rm d}^{\rm iso}$ computed using the continuum and the line intensities differs by $\lesssim$0.3 dex, i.e. a factor $\lesssim$2. Hence, the relationships between continuum and line luminosities seem quite robust. A possible explanation for the larger dispersion in the 5100Å–Hβ case, with respect to the 3000Å–Mg II one, may be that the continuum luminosity at 5100Å is contaminated by the host galaxy.

Both the continuum and the line luminosities in S11 are affected by uncertainties, therefore the distributions shown in Fig. 2 are likely broadened by measurement errors. Thus, the intrinsic dispersion is expected to be smaller than 0.3 dex (a factor of $\sim$2) for Hβ and C IV, and 0.2 dex (a factor of $\sim$1.6) for Mg II. This is yet another evidence that SEDs in most AGN show some degree of universality: the constancy of the continuum to line luminosity ratio at optical wavelengths implies a constant optical continuum to ionizing UV luminosity ratio.

Since the samples in the S11 catalog are dominated by radio–quiet sources (the great majority are undetected in the FIRST survey), we repeat our analysis on radio–loud sources, i.e. those sources for which the radio–loudness parameter[2] is greater than 100. Interestingly, the κ parameters for the radio–loud sub–sample of S11 differ by at most $\sim$5% from the values quoted above.

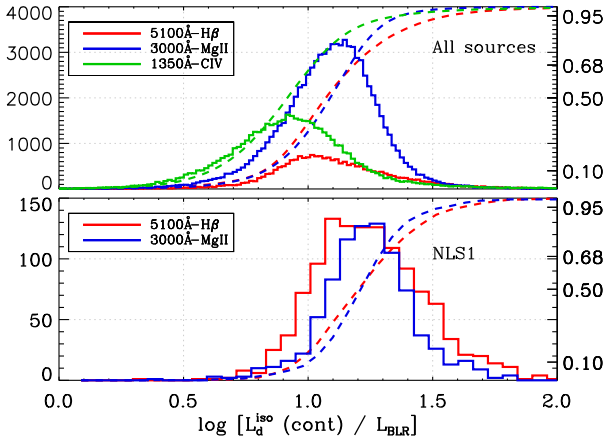

Figure 2. Upper panel: distribution of the κ parameter (Eq. 3 for the three combinations 5100Å–Hβ, 3000Å–Mg II and 1350Å–C IV. Both the continuum and line luminosity estimates are those reported in the S11 catalog. The number of sources in each subsample are 22644, 85514 and 52157 respectively (note that a single source typically belongs to two such subsample). Lower panel: the same as upper panel, for the subsample of Narrow–Line Seyfert 1 sources common to both the S11 and Zhou et al. (2006) catalog.

By using the values given in Eq. 4 and the coefficients to compute the line luminosity $L_{\rm line}$ discussed above, we are able to estimate the total disk luminosity as follows:

$$\begin{aligned} L_{\rm d}^{\rm iso} &= 12\, L({\rm H}\beta)\, \frac{555.8}{22} = 303\, L({\rm H}\beta) \\ L_{\rm d}^{\rm iso} &= 12.5\, L({\rm Mg\,II})\, \frac{555.8}{34} = 204\, L({\rm Mg\,II}) \\ L_{\rm d}^{\rm iso} &= 8.4\, L({\rm C\,IV})\, \frac{555.8}{63} = 74.1\, L({\rm C\,IV}). \end{aligned} \qquad (5)$$

We repeat the above analysis on the subsample of NLS1 sources, that are the focus of our study. In particular, we consider the sources common to both the Zhou et al. (2006) and the S11 catalog (1210 sources). The distributions[3] of the κ parameter are still log–normal, and are shown in the lower panel of Fig. 2. Median values are now $\sim$0.15 dex (i.e. a factor $\sim$1.4) greater:

$$\begin{aligned} &\log\kappa(5100\text{Å} - {\rm H}\beta) = 1.23 \pm 0.23 \\ &\log\kappa(3000\text{Å} - {\rm Mg\,II}) = 1.24 \pm 0.21. \end{aligned} \qquad (6)$$

The uncertainties are of the same order of magnitude. The class of NLS1 sources is therefore characterized by both a

[2] The radio–loudness parameter provides an indication of whether the AGN SED is dominated by radiation at radio frequencies or optical band. Historically, it is defined as the ratio of 5 GHz to optical B–band luminosity (Kellermann et al. 1989). The values we used here are those given in S11, defined as the ratio of flux densities at 6 cm and 2500Å (rest frame).

[3] The 1350Å–C IV case is missing since the SDSS wavelength coverage does not allow to observe both the C IV line and the Hβ line (required to classify the source as a NLS1).

smaller width and a smaller luminosity of lines. The resulting disk luminosities are:

$$L_{\rm d}^{\rm iso} = 424\, L({\rm H}\beta)$$
$$L_{\rm d}^{\rm iso} = 286\, L({\rm Mg\,II}). \quad (7)$$

In order to estimate the accretion disk luminosity using a single spectrum we can use either Eq. 2 (whose uncertainties are ∼20%) or Eq. 7 (whose uncertainties are a factor ∼2). In cases where the observed continuum radiation is dominated by components other than AD, e.g. synchrotron emission from the jet or host galaxy starlight, Eq. 2 would overestimate the disk luminosity. Therefore Eq. 7 is our preferred choice to estimate $L_{\rm d}^{\rm iso}$.

3 THE SAMPLE

The aim of this work is to estimate the black hole masses of the sample of 23 Radio–Loud, Narrow–Line Seyfert 1 sources (RL–NLS1) given in Yuan et al. (2008, hereafter Y08). We identify each source with a sequential index (#1, #2, etc...), following the same order as in Tab. 1 of Y08.

All sources have been spectroscopically observed in the SDSS, and 21 over 23 sources are also in the S11 catalog. The IR photometry at 3.4μm, 4.6μm, 11.6μm, 22.1μm from WISE (Wide–field Infrared Survey Explorer, Wright et al. 2010) is available for all sources. Finally, 21 over 23 sources have photometric measurements by GALEX (Martin et al. 2005), either in the Medium Imaging Survey (MIS), or the All sky Imaging Survey (AIS). We noticed that when multiple GALEX observations were available, we find significant variability in a few cases (#3, #8, #18) possibly due to the jet component. In these cases we chose preferably the MIS photometry with lower luminosity.

The redshifts are in the range z =0.1–0.8, therefore the continuum in the SDSS spectra will likely trace the AD component (§2). The FWHM(Hβ) are less than 2200 km s^{-1}, as required by the definition of NLS1 given in Zhou et al. (2006). The SE virial black hole masses are in the range $\log(M/M_{\odot})$ =6–8, while the Eddington ratio are ℓ =0.5–3 (Yuan et al. 2008). The radio morphology is compact, unresolved on 5″ scale, and the radio loudness (Kellermann et al. 1989) is >100 for all sources.

The overall observational properties are very similar to that of blazars (Yuan et al. 2008), and the γ–ray emission from these sources has been predicted, and later detected in 7 RL-NLS1 sources (Abdo et al. 2009c; Calderone et al. 2011; Foschini 2011), 4 of which are in the Y08 sample. However, these sources show unusually small widths of broad emission lines, and consequently small SE virial black hole mass estimates, when compared to typical blazars.

In order to apply our black hole mass estimation method (§4) to the sources in the sample we need to perform a spectroscopic analysis of the SDSS data. In particular we need to disentangle the host galaxy and/or jet contribution from the AGN continuum, and estimate the emission line luminosities. This procedure is described in the following section.

3.1 Spectral analysis

We used the spectra from the Sloan Digital Sky Survey (SDSS, York et al. 2000), data release 7 (DR7, Abazajian et al. 2009). We dropped spectral bins marked by at least one of the following mask flags:[4] `SP_MASK_FULLREJECT`, `SP_MASK_LOWFLAT`, `SP_MASK_SCATLIGHT`, `SP_MASK_BRIGHTSKY`, `SP_MASK_NODATA`, `SP_MASK_COMBINEREJ`, `SP_MASK_BADSKYCHI`. Also, we dropped 100 bins at the beginning and end of each spectrum, in order to eventually avoid artifacts from instrument or pipeline.

Each spectrum has been de-reddened using the Galactic extinction values estimated from dust IR emission maps in Schlegel et al. (1998), and the extinction law reported in Cardelli et al. (1989) and O'Donnell (1994). We are currently neglecting any intrinsic reddening in the rest–frame of the source. Then we transformed the spectra to the rest frame by assuming isotropic emission (i.e. multiplying the flux by $4\pi D_{\rm L}^2$). The redshift estimates are provided by the SDSS pipeline. Finally, we rebinned each spectrum by a factor of 3 in order to improve the signal to noise ratio, resulting in a spectral resolution of $\lambda/\delta\lambda$ ∼1450 (corresponding to ∼200 km s^{-1}).

The model used to fit the spectra consists of five components:

- a smoothly broken power law to account for the AGN continuum ("AGN continuum" component) ;
- a spiral[5] host galaxy template spectrum from Mannucci et al. (2001) and a power law to (eventually) account for the synchrotron emission from the jet ("galaxy" and "jet" components respectively). The galaxy component has a single free parameter (the overall normalization). The parameters for the jet component are estimated using data from WISE (Wide–field Infrared Survey Explorer, Wright et al. 2010). In particular we use the photometry in the two bands at the longest wavelengths (11μm and 22μm) to estimate the luminosity and the slope of the power law.[6] If the resulting slope is greater than –1 we extrapolate the power law to optical wavelengths and subtract the contribution from the SDSS spectrum. Otherwise we do not consider any jet component. Parameter of the jet component are fixed during the fitting process;
- the iron templates from Vestergaard & Wilkes (2001) (at UV wavelengths) and from Véron-Cetty et al. (2004) (at optical wavelengths);
- a Gaussian profile for each emission line listed in Tab. 1. The FWHM of narrow lines are forced to be in the range 200–1000 km s^{-1}, while that of broad lines are forced in the range 1000–3000 km s^{-1}. Furthermore, the FWHM and velocity offset of the Hβ narrow component is tied to the width and offset of [O III] λ4959 and [O III] λ5007.
- a maximum of 10 additional Gaussian line profiles which are not "a priori" associated to any specific transition. These components are necessary to account for (e.g.) the iron blended emission lines in the range 3100–3500Å (not covered by the above–cited iron templates), or line asymme-

[4] See `http://www.sdss.org/dr7/dm/flatFiles/spSpec.html`.
[5] The results of the spectral fitting procedure do not change significantly by considering the elliptical galaxy template from Mannucci et al. (2001).
[6] In analyzing the source SDSS J094857.32+002225.5 (#5) we also applied an exponential cutoff at $\log[\nu/{\rm Hz}] = 14$ (Abdo et al. 2009b).

Table 1. List of emission lines used in modeling SDSS spectra. Third column (Type) indicates if a broad (B), a narrow (N) or both components are used in the fit.

Line	Wave [Å]	Type	Line	Wave [Å]	Type
C II	2326	B	N I	5199	N
Mg II	2798	BN	He I	5876	BN
Ne V	3426	N	Fe VII	6087	N
O II	3727	N	O I	6300	N
Ne III	3869	N	Fe X	6375	N
H δ	4101	B	N II	6548	N
H γ	4340	BN	H α	6563	BN
O III	4363	N	N II	6583	N
He II	4686	BN	S II	6716	N
H β	4861	BN	S II	6731	N
O III	4959	N	Ar III	7136	N
O III	5007	N			

tries. The FWHM of the additional lines are forced to be in the range 1000–3000 km s^{-1}, except for lines in the range 3100–3500Å for which the upper limit is 10^4 km s^{-1}. A posteriori, we check whether the wavelength range identified by the full width at half maximum of these additional lines contains any of the transition lines listed in Tab. 1. In this case we associate the two components, and numerically compute the line luminosity on the composite line profile.

Results of the spectral fitting are shown in Tab. 2 and Fig. B1.

4 BLACK HOLE MASS ESTIMATION METHOD

The AGN continuum in the rest frame wavelength range 1000–5000Å (or $\log(\nu/\mathrm{Hz})$=14.8–15.5), if interpreted as radiation emitted from a Shakura & Sunyaev (1973) accretion disk (§2), allows to constrain an AD model, and to infer the black hole mass. Once we assume proper values for the inner radius of the disk $R_{\rm in}$ and the viewing angle θ (§4.1), the luminosity and frequency of the peak of the AD spectrum uniquely identify a value of the black hole mass. In the following sections we will discuss two methods to locate the peak of the AD spectrum, and infer the black hole mass and accretion rate. An example of the application of both methods to a specific case will be discussed in §4.3.

4.1 Hypotheses

The methods relies on the following hypotheses, which need to be independently verified:

(i) accretion in AGN occurs through steady–state, geometrically thin, optically thick, non–relativistic accretion disks. The emitted spectrum is well described by an AD model (Shakura & Sunyaev 1973);

(ii) once the galaxy and/or jet contribution has been subtracted, the continuum radiation in the range $\log(\nu/\mathrm{Hz})$=14.8–15.5 (§2) is emitted directly from the accretion disk, i.e. it has not been reprocessed by intervening material, nor it is emitted by some other component;

(iii) the spatial extention of the disk is $R_{\rm in} = 6R_{\rm g}$, corresponding to a radiative efficiency $\eta \sim 0.1$. The outer radius of the disk $R_{\rm out} = 2\times10^3 R_{\rm g}$ is not critical, since at frequencies much smaller than $\nu_{\rm p}$ the AD spectrum will always be hidden by other emitting components. The assumption for $R_{\rm in}$, on the other hand, is more critical, since our black hole mass estimates show a linear dependence on this value (case (v) of §A2);

(iv) the relation between disk luminosity and its "isotropic equivalent" counterpart is $L_\nu^{\rm iso} = \langle 2\cos\theta\rangle L_\nu$ (Eq. A16). Since we are interested in Type 1 AGN the viewing angle is in the range 0–45 deg (i.e. the aperture of the obscuring torus, Calderone et al. 2012). The averaged de–projection factor is thus $\langle 2\cos\theta\rangle \sim 1.7$ (Eq. A15, A16), corresponding to a viewing angle of ∼30 deg.

The AD model has four parameters: M, $\dot{M}$, $R_{\rm in}$ and $\cos\theta$ (§A3). With the assumptions discussed above, the remaining unknown parameters are the black hole mass M and the accretion rate $\dot{M}$.

4.2 Procedure

Usually the localization of the peak of the AD spectrum is not accessible by using a single instrument, requiring optical/UV multiwavelength observations. When these observations are available it is possible to constrain the AD model, and estimate the frequency $\nu_{\rm p}$ and luminosity $\nu_{\rm p}L_{\nu_{\rm p}}^{\rm iso}$ of the peak. The latter can then be used to infer the total disk luminosity $L_{\rm d}^{\rm iso}$ (Eq. A10). Finally, the black hole mass and the accretion rate can be estimated as follows:

$$\frac{M}{10^9 M_\odot} = 1.44 \left(\frac{\nu_{\rm p}}{10^{15}\ \mathrm{Hz}}\right)^{-2} \left(\frac{L_{\rm d}^{\rm iso}}{\langle 2\cos\theta\rangle \times 10^{45}\ \mathrm{erg\ s^{-1}}}\right)^{1/2}$$
$$\frac{\dot{M}}{M_\odot\ \mathrm{yr}^{-1}} = 0.21 \left(\frac{L_{\rm d}^{\rm iso}}{\langle 2\cos\theta\rangle \times 10^{45}\ \mathrm{erg\ s^{-1}}}\right) \quad (8)$$

The uncertainties on these results can be estimated by propagating the uncertainties in the $\nu_{\rm p}$ and $\nu_{\rm p}L_{\nu_{\rm p}}^{\rm iso}$ parameters in the above equations. Hence, whenever the data allow to constrain the location of the peak of the AD spectrum, the accuracy of the black hole mass estimate is determined only by the accuracy of the data points (e.g. Sbarrato et al. 2012). When UV observation are not available (or not reliable) the location of the peak cannot be constrained, and we must resort to an alternative method.

4.2.1 The `LINE` *procedure*

Here we propose a new method for the AD modeling which relies on broad line luminosities to estimate the total disk luminosity. Fig. 3 illustrates the method. We use Eq. 7 to estimate $L_{\rm d}^{\rm iso}$. When both the Hβ and Mg II line luminosities were provided by our spectral fitting (§3.1) we considered the average of the resulting disk luminosities. This enables us to estimate a value for the luminosity of the peak $\nu_{\rm p}L_{\nu_{\rm p}}^{\rm iso}$ (Eq. A10), i.e. to fix a "ceiling" in the νL_ν representation (black dashed line in Fig. 3): the peak of the AD spectrum must lie on this line. Then we use observations from a single instrument (SDSS) to constrain the peak frequency $\nu_{\rm p}$, which is related to the black hole mass. In particular, we shift the AD spectrum horizontally (green arrow), until the AD spectrum reproduces the AGN continuum identified in §3.1. Note that the model to be compared with data in Fig. 3 is an

Table 2. Results of the spectral fitting for the 23 RL–NLS1 sources in Yuan et al. (2008) catalog. Columns are: (1) source numeric identifier; (2) SDSS name of the source; (3) redshift; (4) luminosity and error of the Hβ emission line (both the broad and narrow components); (5) luminosity and error of the Mg II emission line (both the broad and narrow components); (6) wavelength λ_0 and (7) luminosity $\lambda_0 L_{\lambda_0}$ used to constrain the `LINE` model (see §4.2.1); (8) jet component (extrapolated from WISE data to wavelength λ_0) to AGN continuum luminosity ratio.

#	SDSS Name	z	$\log \frac{L(\mathrm{H}\beta)}{\mathrm{erg\ s^{-1}}}$	$\log \frac{L(\mathrm{Mg\,II})}{\mathrm{erg\ s^{-1}}}$	$\log \frac{\lambda_0}{\mathrm{\AA}}$	$\log \frac{\lambda_0 L_{\lambda_0}}{\mathrm{erg\ s^{-1}}}$	$\frac{L_{\mathrm{J},0}}{L_{\lambda_0}}$
1	J081432.11+560956.6	0.509	42.96 ± 0.01	42.99 ± 0.02	3170	45.11	—
2	J084957.98+510829.0	0.583	42.29 ± 0.12	42.52 ± 0.04	3039	43.58	5.67
3	J085001.17+462600.5	0.523	42.48 ± 0.04	42.51 ± 0.03	3157	44.61	0.13
4	J090227.16+044309.6	0.532	42.61 ± 0.03	42.93 ± 0.02	3127	44.67	0.07
5	J094857.32+002225.5	0.584	42.81 ± 0.03	42.85 ± 0.03	3039	45.15	0.00
6	J095317.09+283601.5	0.657	42.54 ± 0.03	42.84 ± 0.02	2893	44.88	0.10
7	J103123.73+423439.3	0.376	42.31 ± 0.02	—	3486	44.12	—
8	J103727.45+003635.6	0.595	42.52 ± 0.05	42.31 ± 0.04	3020	44.73	—
9	J104732.68+472532.1	0.798	43.10 ± 0.03	43.04 ± 0.04	2674	45.15	0.12
10	J111005.03+365336.3	0.630	42.36 ± 0.04	42.59 ± 0.03	2944	44.26	0.01
11	J113824.54+365327.1	0.356	42.26 ± 0.01	—	3547	43.87	0.64
12	J114654.28+323652.3	0.465	42.68 ± 0.01	42.65 ± 0.03	3285	44.75	—
13	J123852.12+394227.8	0.622	42.41 ± 0.05	42.48 ± 0.03	2961	44.59	0.02
14	J124634.65+023809.0	0.362	42.43 ± 0.02	—	3525	44.66	0.05
15	J130522.75+511640.3	0.785	43.79 ± 0.01	43.47 ± 0.01	2692	45.74	0.47
16	J143509.49+313147.8	0.501	42.43 ± 0.02	42.65 ± 0.03	3203	44.46	0.72
17	J144318.56+472556.7	0.703	42.82 ± 0.04	43.24 ± 0.02	2826	45.42	0.15
18	J150506.48+032630.8	0.408	41.90 ± 0.03	42.55 ± 0.04	3407	44.39	0.14
19	J154817.92+351128.0	0.478	42.84 ± 0.01	42.93 ± 0.02	3249	45.05	0.06
20	J163323.58+471859.0	0.116	41.66 ± 0.02	—	4303	43.74	0.43
21	J163401.94+480940.2	0.494	42.45 ± 0.02	42.02 ± 0.02	3213	44.56	0.14
22	J164442.53+261913.2	0.144	41.86 ± 0.01	—	4200	43.95	0.25
23	J172206.03+565451.6	0.425	42.55 ± 0.01	42.64 ± 0.03	3370	44.68	0.04

"isotropic equivalent" AD spectrum (Eq. A13). The resulting AD model (red solid line) provides an estimate for ν_{p}, to be used (along with $L_{\mathrm{d}}^{\mathrm{iso}}$) in Eq. 8 to infer the black hole mass and accretion rate. Finally, we compute the Eddington ratio ℓ using the luminosity of the disk:[7] $\ell = L_{\mathrm{d}}/L_{\mathrm{Edd}}$.

The main source of uncertainty in the process is the uncertainty in the disk luminosity $L_{\mathrm{d}}^{\mathrm{iso}}$ (a factor 2, §2.2). This uncertainty is shown as a grey shade in Fig. 3. In order to evaluate a confidence interval for our estimates of M we repeat the whole process requiring the peak luminosity of the AD spectrum to lie respectively at the top and the bottom of the grey stripe. The resulting AD models (dot–dashed red lines) provide respectively the lower and upper limits of the confidence interval on the black hole mass, which typically is ±0.5 dex. In some case these limiting AD models are too distant from the data to provide a meaningful description of the AGN continuum. This occurs typically for the low luminosity solution, corresponding to the upper limit in black hole mass (e.g. §4.3). In these cases a visual inspection would reduce the thickness of the grey stripe, and hence the uncertainty on the black hole mass.

Further sources of uncertainties are the assumption on the radiative efficiency $\eta \sim 0.1$ and on the viewing angle $\theta \sim 30$ deg (§4.1). The uncertainty due to the former can be estimated by considering that our black hole mass estimate is $M \propto \eta$ (case (v) of §A2), and that the actual value of η is expected to range from ∼6% (for non–rotating black hole) to at most ∼30% (for a spin parameter $a = Jc/GM^2 = 0.998$, Thorne 1974). Therefore the uncertainty on the black hole mass due to the uncertainty on η (and ultimately on the black hole spin) is +0.5/-0.2 dex. If we consider the possibility that the black hole can be maximally counter–rotating (with respect to the direction of accretion) then the uncertainty on the black hole mass due to the uncertainty on η becomes ±0.5 dex. The uncertainty due to the assumption on the viewing angle can be estimated by propagating the error in Eq. 8. Typically, this is negligible compared to the uncertainties discussed above, being at most 0.04 dex (a factor ∼1.1), provided $\theta_{\mathrm{max}} < 45$ deg. The uncertainties due to $L_{\mathrm{d}}^{\mathrm{iso}}$ and η are likely uncorrelated, therefore, the maximum expected uncertainty for the black hole mass estimate is ±0.7 dex.

The `LINE` procedure can be implemented without any fitting procedure, provided we have an estimate for the broad line luminosities and the AGN continuum (§3.1). The search for the peak frequency can be implemented by identifying a wavelength λ_0 and the corresponding luminosity of the AGN continuum $\lambda_0 L_{\lambda_0}$, and requiring the AD spectrum to match this luminosity at the same wavelength. A comparison between the resulting AD model and the AGN continuum can be performed "a posteriori" in order to assess the reliability of the black hole mass estimate (§4.2.2). For SDSS spectra of sources with $z < 0.8$ the value of λ_0

[7] We are neglecting the contribution from the torus in computing the Eddington luminosity since it is reprocessed radiation from the disk. If we had used the bolometric luminosity L_{bol}, instead of L_{d}, the resulting value would be overestimated by a factor 3.4 on average (Eq. 1 and A16).

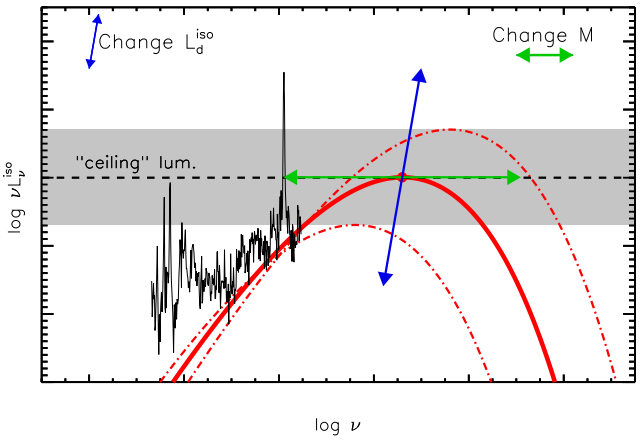

Figure 3. The `LINE` black hole mass estimation procedure: the SDSS source spectrum (black line) is analyzed with our fitting procedure (§3.1) in order to estimate the broad line luminosities. Then we use Eq. 7 to estimate $L_{\rm d}^{\rm iso}$. This is equivalent to estimate a value for the luminosity of the peak $\nu_{\rm p}L_{\nu_{\rm p}}^{\rm iso}$ (Eq. A10), i.e. to fix a "ceiling" in the νL_ν representation (black dashed line). Then we use the SDSS spectrum to constrain the peak frequency $\nu_{\rm p}$, which is related to the black hole mass. In particular, we shift the AD spectrum horizontally (green arrow), until the AD spectrum reproduces the AGN continuum identified in §3.1. The resulting AD model (red solid line) provides an estimate for $\nu_{\rm p}$, to be used (along with $L_{\rm d}^{\rm iso}$) in Eq. 8 to infer the black hole mass and accretion rate. The uncertainty in the disk luminosity $L_{\rm d}^{\rm iso}$ (a factor 2, §2.2) is shown as a grey shade. In order to evaluate a confidence interval for our estimate of M we repeat the whole process requiring the peak luminosity of the AD spectrum to lie respectively at the top and the bottom of the grey stripe. The resulting AD models (dot–dashed red lines) provide respectively the lower and upper limits of the confidence interval on the black hole mass.

has been chosen empirically as follows:

$$\lambda_0 = \lambda_{\rm min}\left(\frac{\lambda_{\rm max}}{\lambda_{\rm min}}\right)^{0.25}$$

where $\lambda_{\rm min}$ and $\lambda_{\rm max}$ are the minimum and maximum rest–frame wavelengths of the SDSS spectrum. This value is sufficiently close to the short wavelength edge in order to minimize the contamination from other continuum components (either galaxy or jet); λ_0 is also sufficiently far from the shortest available wavelength, at which the estimated luminosity may be unreliable due to noise and/or edge artifacts. Following these prescriptions the `LINE` method can be efficiently implemented as an automated procedure on large samples.

4.2.2 The `BEST` *procedure*

In order to assess the reliability of the `LINE` procedure we proceed with a visual localization of the AD spectrum peak using the SDSS and GALEX observations. Photometry from GALEX has been de–reddened following the same procedure as for the optical SDSS spectra (§3.1). In addition, when a jet component is considered in the spectral fitting, we compute the jet–subtracted GALEX photometry. We can not exclude that further absorption took place either in the AGN environment or the intervening medium, therefore we consider the photometry as lower limits to the actual rest–frame luminosity. Note that SDSS and GALEX data are not simultaneous, therefore it may happen that these data sets trace the source in two different state of emission, e.g. a disk or a jet dominated state (Calderone et al. 2012).

For each source we require the slope of the AD spectrum to match as close as possible the slope in the AGN continuum (§3.1), and to lie above the (jet–subtracted) GALEX photometry. A few exceptions to these rules will be considered in §6. Since this is a manually tuned AD model we give no error associated to the corresponding black hole mass.

4.3 Example of application of the methods

As an example we discuss the case of SDSS J09531.7.09+283601.5 (#6), in Fig. 4. The WISE photometry is shown with black filled circles. The spectral fit (§3.1) is shown as a black line, while the AGN continuum component is shown as cyan line. The jet power law extrapolation from IR data is shown as a purple line. The GALEX photometry and their jet subtracted counterparts are shown as open circles and "+" symbols respectively. The disk luminosity $L_{\rm d}^{\rm iso}$ with its uncertainty of a factor 2 is shown as a grey stripe: the peak of the AD model must lie within this region. The grey dashed grid shows the location of peaks for AD models with values of black hole mass and Eddington ratio shown respectively below and above the grey stripe.

By applying our black hole mass estimation methods we identify the `LINE` and `BEST` AD models, shown with a red and orange solid line respectively. Both AD models provide a rather good representation of the AGN continuum. The `BEST` AD model, however, needs a slightly higher luminosity than the `LINE` model in order to lie above the (jet–subtracted) GALEX photometry. Note that the observed spectrum (black line) has a significantly lower spectral slope (i.e. it is "redder") than the AGN continuum, because of the host galaxy and jet contributions. Having considered these components in the spectral analysis allows us to reveal the real AGN continuum (cyan line) whose slope agrees with our AD spectrum.

In order to evaluate the uncertainty on the `LINE` black hole mass we repeat the procedure by requiring the AD model to peak at the top and the bottom of the grey stripe. The resulting AD models (shown with dot–dashed red lines) are found to bracket the real case: the lower one cannot account for the AGN continuum, while the higher one is significantly above the GALEX photometry. This situation often occurred during the analysis of the sources (§6), therefore our black hole mass uncertainties are rather conservative.

Our AD models can be compared with those corresponding to the SE virial masses and bolometric luminosities reported in the Y08 and S11 catalogs (green and blue lines). We consider the disk luminosity as computed using Eq. 1. Note that our peak luminosities are very similar to those of Y08 and S11, since this is the condition we required (on average) to calibrate Eq. 7. However, these models do not provide a good description of the AGN continuum because their peak frequencies lie ∼0.25 dex above our estimates of $\nu_{\rm p}$, therefore our black hole mass estimates are 0.5 dex (a factor ∼3, Eq. A8) greater than the virial ones. The possible reasons to explain such differences will be discussed in §6.1.

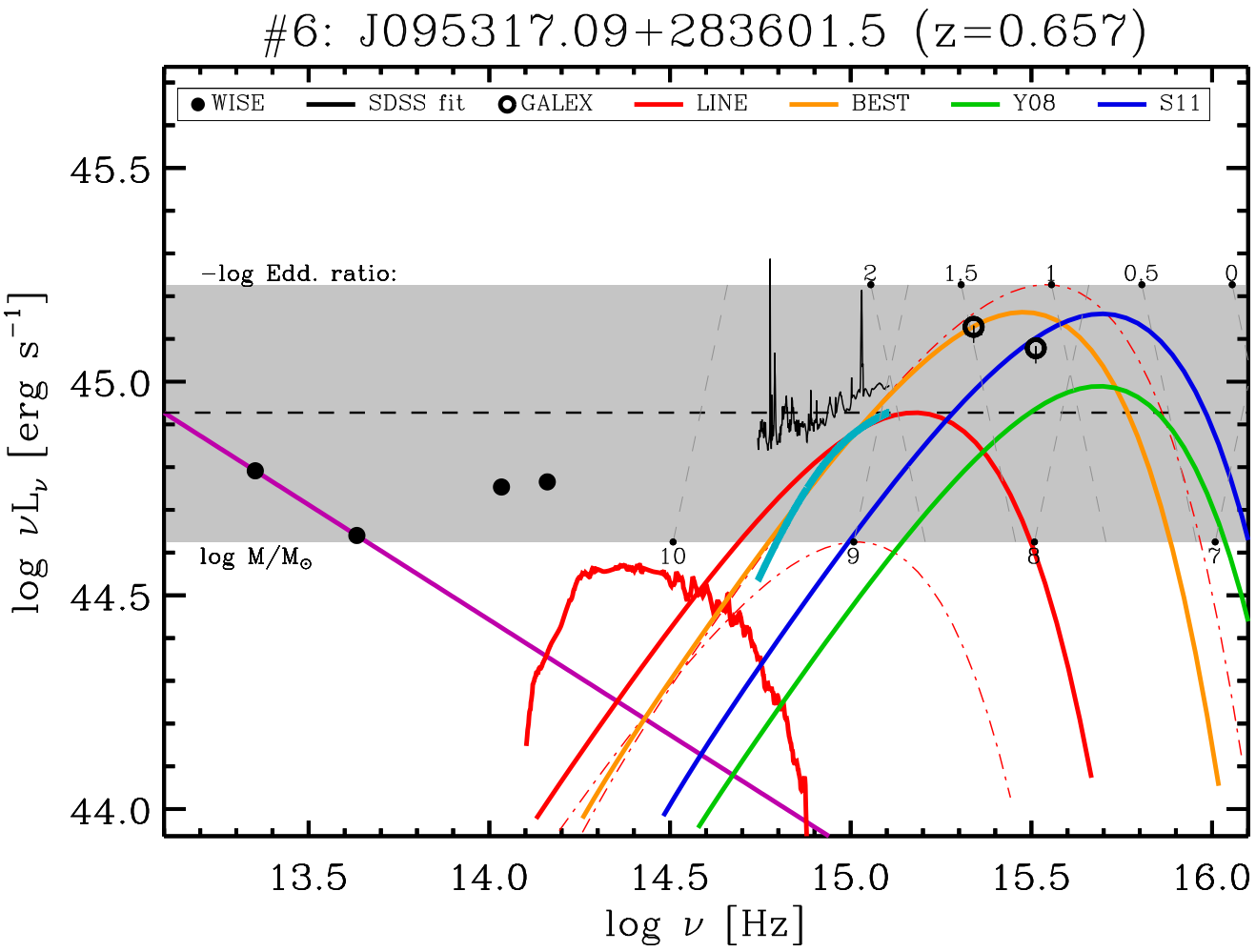

Figure 4. Application of the black hole mass estimation methods to the source SDSS J09531.7.09+283601.5 (#6). The WISE photometry is shown with black filled circles. The spectral fit (§3.1) is shown as a black line, while the AGN continuum component is shown as cyan line. The jet power law extrapolation from IR data is shown as a purple line. The GALEX photometry and their jet subtracted counterparts are shown as open circles and "+" symbols respectively. The disk luminosity $L_{\rm d}^{\rm iso}$ with its uncertainty of a factor 2 is shown as a grey stripe: the peak of the AD model must lie within this region. The grey dashed grid shows the location of peaks for AD models with values of black hole mass and Eddington ratio shown respectively below and above the grey stripe. The `LINE` (§4.2.1) and `BEST` (§4.2.2) AD models are shown with a red and orange solid line respectively. In order to evaluate the uncertainty on the `LINE` black hole mass we repeat the procedure by requiring the AD model to peak at the top and the bottom of the grey stripe. The resulting AD models are shown with dot–dashed red lines.

5 RESULTS

We analyzed the data from the 23 RL–NLS1 sources of the Y08 catalog. The spectral analysis (§3.1) of each individual source is shown in Fig. B1. The results are summarized in Tab. 2. The fitting models are in good agreement with data with reduced χ^2 in the range 1.16–1.86. Also, the jet contribution at optical/NUV wavelengths is typically negligible, except for the #2, #11, #15, #16, #20 and #22 sources.

The results of our black hole mass estimation methods (§4) are shown graphically in Fig. C1 (adopting the same notation as in Fig. 4). The results are summarized in Tab. 3. The AD models identified by the `LINE` procedure provide a rather good description of the AGN continuum in 17 over 23 cases (indicated with a blank in the second column of Tab. 3). The remaining 6 sources cannot be modeled with an AD spectrum, and are considered "bad cases" (indicated with a "*" symbol in the second column of Tab. 3, see §6 for a discussion of these sources). These sources will not be considered in the following analysis.

The comparison between the black hole mass estimates for the `LINE` and `BEST` AD models are shown in Fig. 5. The mean value for the ratio of the two mass estimates is:

$$\left\langle \log \frac{M[\texttt{LINE}]}{M[\texttt{BEST}]} \right\rangle = 0.07 \pm 0.37 \qquad (9)$$

The two black hole mass estimates are therefore compatible, within the uncertainties associated to the `LINE` procedure (§4.2.1).

In Fig. 6 we show the comparison between the black hole masses from the AD models (`LINE` in upper panels, `BEST` in lower panels) and the black hole masses from SE virial method, as given in the Y08 (left panels) and S11 (right panels) catalogs. The uncertainty associated to SE

Table 3. Results of our black hole mass estimation method. Columns are: (1) source numeric identifier; (2) flag to indicate if the AD "signature" (i.e. the slope $\alpha_\nu > -1$ a t optical wavelengths, see §6) is missing. (3) peak frequency of the AD model, (4) black hole mass estimate (with its uncertainties) and (5) Eddington ratio for the AD model identified by our automatic procedure (`LINE` model); (6), (7), (8) corresponding quantities for the `BEST` model; single epoch (SE) virial black hole mass estimate given in the (9) Y08 and (10) S11 catalogs.

		Method			**Best**			**Y08**	**S11**
#	Bad	$\log \frac{\nu_{\rm p}}{\rm Hz}$	$\log \frac{M}{M_\odot}$	ℓ	$\log \frac{\nu_{\rm p}}{\rm Hz}$	$\log \frac{M}{M_\odot}$	ℓ	$\log \frac{M}{M_\odot}$	$\log \frac{M}{M_\odot}$
1		15.2	$8.8\ (+0.4\ ,-0.5\ )$	0.022	15.5	8.4	0.084	8.0	8.1
2	*	—	—	—	—	—	—	7.4	8.0
3		15.3	$8.5\ (+0.4\ ,-0.5\ )$	0.014	15.1	8.8	0.006	7.2	7.5
4		15.5	$8.2\ (+0.6\ ,-0.4\ )$	0.059	15.3	8.5	0.019	7.7	8.0
5		15.0	$9.2\ (+0.0\ ,-0.6\ )$	0.006	15.1	9.1	0.010	7.5	7.8
6		15.2	$8.8\ (+0.2\ ,-0.6\ )$	0.012	15.5	8.3	0.062	7.8	7.9
7	*	—	—	—	—	—	—	7.3	7.6
8		15.0	$9.0\ (+0.0\ ,-0.7\ )$	0.004	15.0	9.1	0.004	7.3	8.5
9	*	—	—	—	—	—	—	8.1	8.2
10	*	—	—	—	—	—	—	7.1	9.0
11	*	—	—	—	—	—	—	7.1	7.6
12		15.3	$8.6\ (+0.5\ ,-0.5\ )$	0.020	15.1	8.8	0.008	7.8	7.9
13		15.2	$8.5\ (+0.3\ ,-0.5\ )$	0.012	15.4	8.2	0.037	6.8	7.5
14		15.2	$8.7\ (+0.3\ ,-0.5\ )$	0.009	15.2	8.7	0.011	7.3	7.7
15		15.4	$8.8\ (+0.6\ ,-0.4\ )$	0.110	15.2	9.2	0.049	8.5	8.5
16		15.5	$8.1\ (+0.7\ ,-0.4\ )$	0.037	15.1	8.8	0.008	7.5	7.6
17		15.0	$9.3\ (+0.0\ ,-0.5\ )$	0.009	15.6	8.4	0.193	7.8	8.3
18		15.2	$8.5\ (+0.4\ ,-0.5\ )$	0.009	15.4	8.3	0.021	6.6	7.6
19		15.2	$8.9\ (+0.2\ ,-0.6\ )$	0.014	15.3	8.7	0.027	7.9	8.0
20	*	—	—	—	—	—	—	6.3	—
21		15.0	$9.0\ (+0.0\ ,-0.8\ )$	0.003	15.0	8.9	0.004	7.4	7.9
22		15.3	$8.3\ (+0.6\ ,-0.4\ )$	0.007	15.3	8.2	0.008	6.9	—
23		15.3	$8.6\ (+0.5\ ,-0.5\ )$	0.016	15.5	8.1	0.079	7.4	7.6

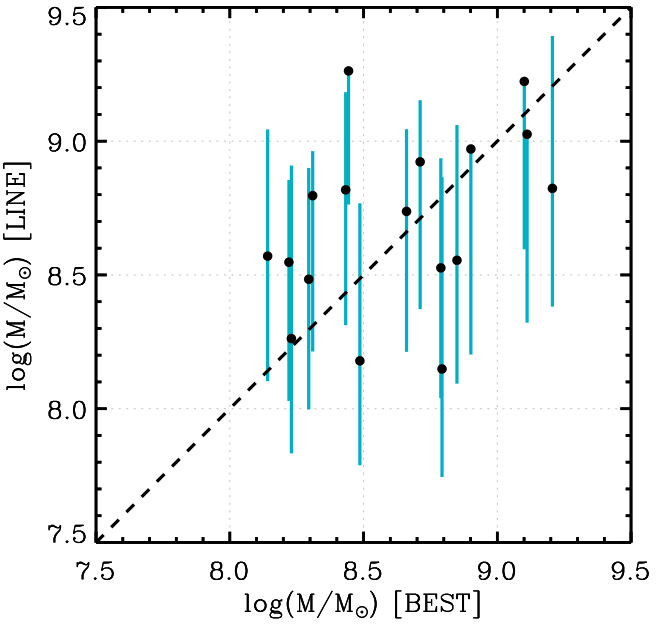

Figure 5. Comparison between black hole mass estimates obtained using the `LINE` and `BEST` procedures. Since the `BEST` estimate is a manually tuned AD model we give no error associated to the corresponding black hole mass.

virial mass is assumed to be 0.5 dex. In Fig. 7 we show the histogram of the ratio of our black hole mass estimates to the SE virial ones from the Y08 (left panel) and S11 (right panel) catalogs. The mean values for the ratio of the mass estimates are:

$$\left\langle \log \frac{M[\texttt{LINE}]}{M[\text{Y08}]} \right\rangle = 1.2 \pm 0.5 \qquad \left\langle \log \frac{M[\texttt{LINE}]}{M[\text{S11}]} \right\rangle = 0.8 \pm 0.3$$
$$\left\langle \log \frac{M[\texttt{BEST}]}{M[\text{Y08}]} \right\rangle = 1.1 \pm 0.4 \qquad \left\langle \log \frac{M[\texttt{BEST}]}{M[\text{S11}]} \right\rangle = 0.8 \pm 0.3 \tag{10}$$

The mean values are of the same order (or even greater) than the maximum uncertainty associated to the `LINE` black hole mass estimate (0.7 dex, §4.2.1), therefore our black hole mass estimates are not compatible with the SE virial ones.

6 DISCUSSION

As discussed in §2, the characteristic disk spectral slope $\alpha_\nu = 1/3$ cannot be directly observed in AGN SED. However for values of the black hole mass $\log(M/M_\odot) \gtrsim 8$ and Eddington ratio $\ell \lesssim 1$, the peak of the AD spectrum is (in principle) observable. Indeed, for 17 over 23 sources considered here, the SDSS continuum show an increasing trend in the νL_ν representation (slope $\alpha_\nu > -1$) at $\log(\nu/\text{Hz}) \gtrsim 14.8$, where the accretion disk is expected to dominate over other emitting components. Assuming that the observed BBB is actually radiation emitted directly from the accretion disk,

the slope $\alpha_\nu > -1$ at $\log(\nu/\mathrm{Hz}) \gtrsim 14.8$ becomes the "signature" of the presence of the AD component. In the considered sample (§3) 17 sources over 23 show such signature (the remaining six "bad" cases will be discussed below). Our spectral fitting procedure (§3.1) reveals an emission component that is well described by an AD model, although this has not been included "a priori" in our fitting model. Therefore, observational data are in agreement with hypothesis (i), as discussed in §4.1. Furthermore, the absorption column densities N_H, as estimated from X–ray spectral fitting, are compatible with the Galactic values (Yuan et al. 2008; Grupe et al. 2010). Hence, we expect the radiation we observe not to be re–processed by any intervening medium, as assumed in hypothesis (ii) (§4.1). Furthermore, we expect the contribution from other emitting components, such as host galaxy or jet, to be negligible at frequencies where our AD models are constrained ($\log(\nu/\mathrm{Hz}) \gtrsim 14.8$). In particular, the slopes in the AGN continuum component ($\alpha_\nu > -1$) is incompatible with the ones inferred from the galaxy template of Mannucci et al. (2001). Also, the jet component is expected to decay at frequencies above a cutoff frequency of $\log(\nu/\mathrm{Hz}) \lesssim 15$, as in typical Flat Spectrum radio–quasars or powerful blazars (Ghisellini et al. 2010).

The AD models identified by the `LINE` procedure (§4.2.1) for the 17 "good" sources provide a rather good description of the AGN continuum (Fig. C1). In particular, the AGN continuum slopes in the frequency range covered by SDSS are in good agreement with the ones from `LINE` AD models (red solid lines). Also, the two limiting solutions (dot–dashed red lines) likely bracket the real case, providing a robust estimate of our uncertainties. The average uncertainty on the black hole mass estimates are of the order of ± 0.5 dex (Tab. 3). By taking into account the uncertainties due to hypotheses (iii) and (iv) (radiative efficiency $\eta \sim 0.1$ and viewing angle $\theta \sim 30$ deg) we obtain a maximum uncertainty of $\sim$0.7 dex (§4.2.1).

In order to further assess the reliability of the `LINE` black hole mass estimates we considered the `BEST` AD models, identified by visually tuning the $L_\mathrm{d}^\mathrm{iso}$ and ν_p parameters in order to achieve the best possible match between the AGN continuum identified in §3.1 and the GALEX photometry. In a few cases we had to relax these requirements, as discussed below:

- the assumption that we can reliably estimate the jet contribution at optical/UV wavelengths by extrapolating a power law from the WISE photometry (§3.1) may not be correct. For the #15 and #16 sources this assumption does not apply since the power law extrapolation (purple line) lies above the WISE photometry at shorter wavelengths (note that the error bars are smaller than the symbol in the plot). Source #5 would also falls in this class if the cutoff of synchrotron radiation at $\sim 10^{14}$ Hz (§3.1) is neglected, since jet extrapolation would intercept optical SDSS data. In order to identify the `BEST` AD model for the #15 and #16 sources we used the continuum observed in SDSS data (black solid lines in Fig. C1) rather than the jet–subtracted one (cyan lines) as requirement at optical wavelengths. For #16 we obtained a good agreement between the `BEST` model and GALEX photometry. Lack of such agreement for #15 will be discussed below. A similar situation (jet component overestimated at optical/NUV wavelengths) possibly occurs also for source #22. In order to be conservative, for this source we retained the original constraints to identify the `BEST` model. For the other sources the jet extrapolation is marginal at optical/NUV wavelengths (Tab. 2), hence the assumption discussed here has a negligible effect.
- for the #5 and #15 sources the GALEX photometry does not follow the extrapolation from the SDSS slope. Therefore a single AD model is not compatible with both the SDSS and GALEX observations. This may be a consequence of source variability, since the SDSS and GALEX data are not simultaneous. Indeed, we found significant variability in GALEX photometry in a few sources (§3.1). In particular, source #5 is known to be a variable source (Abdo et al. 2009a,b; Foschini et al. 2011). In these cases the `BEST` model is computed relaxing the requirement of taking GALEX photometry into account, and using only the SDSS data as guidelines.
- for the #8 and #21 sources the SDSS and GALEX data appear to trace the peak of the AD spectrum. For these sources we neglected the jet component. Note that the `BEST` AD model for these sources provide a robust estimate of the black hole mass, since the peak of the AD spectrum has been directly observed.

The `BEST` AD models are in good agreement with the `LINE` ones. In particular, note that the peak in `BEST` AD spectra lie inside the grey stripes for all sources except #17. Hence, the Eq. 7 are well calibrated. The resulting `BEST` black hole mass estimates are compatible the `LINE` ones (Eq. 9, Fig. 5). Also, the scatter in Fig. 5 (0.4 dex) is compatible with the uncertainty on the `LINE` estimates due to our ignorance on $L_\mathrm{d}^\mathrm{iso}$ (0.5 dex, §4.2.1). This provides further support for the reliability of the `LINE` black hole mass estimates. We conclude that, under the assumptions discussed in §4.1 our `LINE` procedure provides a reliable estimate of the black hole mass, within the quoted uncertainties.

In six cases the `LINE` method do not provide an acceptable description of data (sources marked with a "*" symbol in the second column of Tab. 3. For these sources the observed SDSS continuum does not show an increasing trend (in the νL_ν representation) at $\log(\nu/\mathrm{Hz}) \gtrsim 14.8$. In two cases the SDSS continuum are dominated by the jet and/or host galaxy emission (#2 and #11), and the AD spectrum is not directly visible. In four cases (#7, #9, #10 and #20) the observed SDSS continuum appears "flat" in the νL_ν representation, with no hints for a change of slope. Although the jet–subtracted continuum (cyan line) suggests the presence of an AD spectrum, this decomposition strongly depends on the assumption that the extrapolation of the jet component from IR data is also valid at optical wavelengths. In order to be conservative, we mark these sources as "bad", and neglect them in our analysis.

6.1 Comparison with SE virial mass estimates

The comparison with the SE virial mass reveals a systematic discrepancy between our mass estimate and those from the Y08 and S11 catalogs (Fig. 6 and 7). Although the discrepancy ($\gtrsim$0.7 dex, Eq. 10) is of the same order of the maximum uncertainty associated to the `LINE` procedure (§4.2.1), it appears systematic. Therefore our black hole mass estimates are not compatible with the virial ones given in the Y08

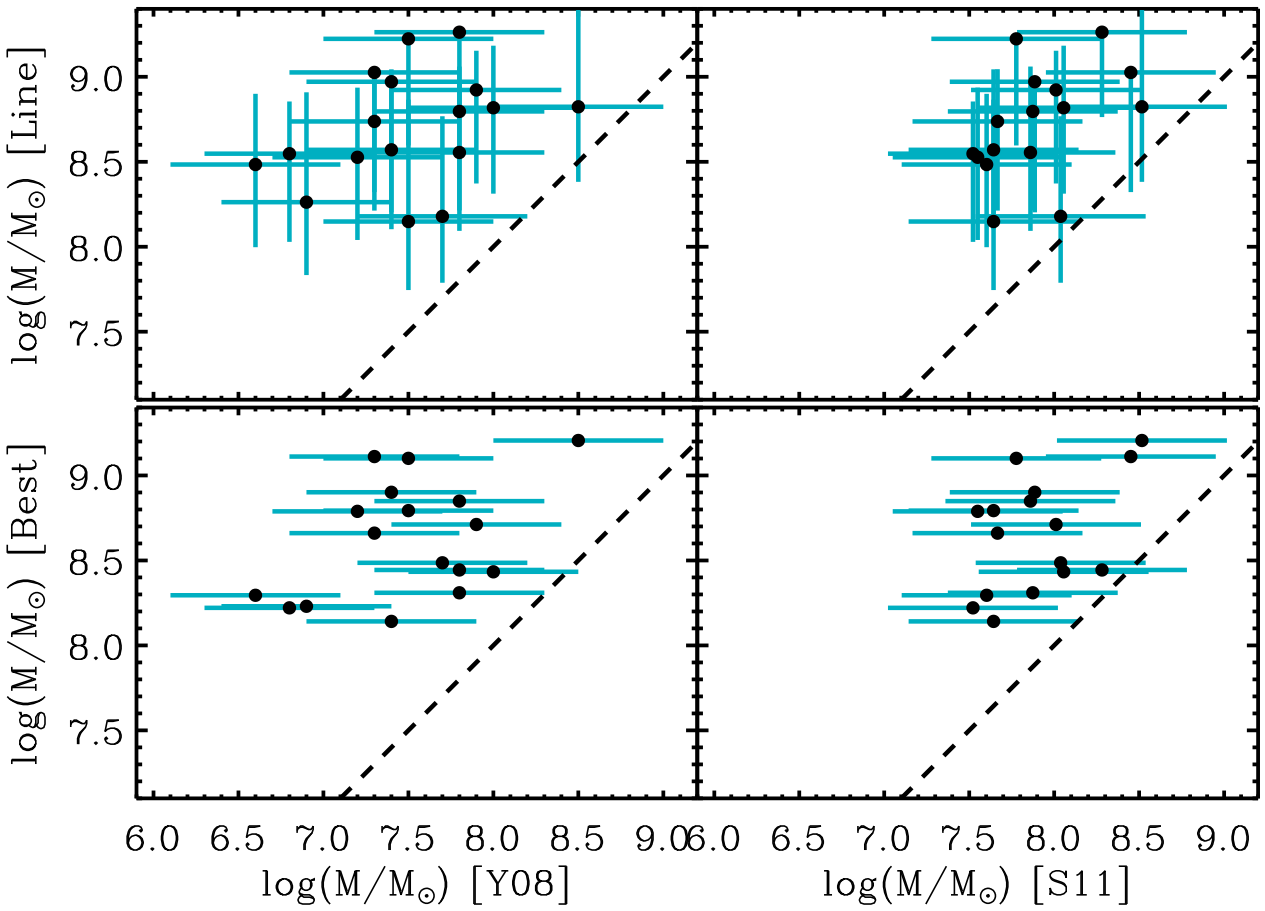

Figure 6. Comparison between black hole mass estimates of AD models identified by our procedures (`LINE` models, upper panels, `BEST` models lower panels) and single epoch (SE) virial masses as given in the Y08 (left panels) and S11 (right panels) catalogs. The uncertainty associated to SE virial mass is 0.5 dex.

and S11 catalogs. On average, our black hole masses turn out to be a factor ∼6 (0.8 dex) greater than virial ones. A possible explanation for this black hole mass discrepancy may involve a radiative efficiency which is a factor ∼6 lower than assumed. However, a value of $\eta \sim 0.02$ is lower than the minimum efficiency expected for accretion onto a maximally counter–rotating black hole (~ 0.03). Notice that the AD spectrum suggests that the accretion disk is still in the "radiatively efficient" regime: half the gravitational energy gained by matter at each radius is locally emitted as radiation, i.e. it is not advected into the hole.

The mass discrepancy is not due to an inaccurate estimation of the jet contribution at optical/NUV wavelengths. If the actual jet contribution is lower than estimated, the corresponding AGN continuum luminosity ($\lambda_0 L_{\lambda_0}$ (Tab. 2) would correspondingly be higher. The "ceiling" luminosity level, on the other hand, are not affected by the presence of the jet, since it relies on line luminosities. In order to reproduce an higher $\lambda_0 L_{\lambda_0}$, retaining the same peak luminosity, the `LINE` AD model must shift to lower frequencies. Therefore, if the actual jet contribution is lower than estimated, we would have obtained greater `LINE` black hole mass estimates, and greater discrepancy with SE virial masses. Furthermore, the mass discrepancy is not due to having neglected the general relativistic corrections in the AD model. As discussed in §A4, the AD model used throughout this work mimics the more sophisticated general relativistic one with $\eta_{\rm gr} \sim 0.1$, as long as frequencies below the peak are concerned.

We speculate that a possible explanation for the mass discrepancy is a selection effect in calibrating the SE virial method. The virial method relies on the calibration of both a BLR size–continuum luminosity relation and of a virial factor (Park et al. 2012). However, the sample used to perform the calibration consists of a few dozens of sources: the ones that has been reverberation mapped. As a consequence, the calibration of the method may be biased by selection effects. In particular, the method may provide significantly underestimated black hole masses if the BLR has a flat disk–like geometry, and it is seen almost face–on (Decarli et al. 2011). If these conditions apply, then the discrepancy between our mass estimates and the virial ones would be greater (on average) for AGN showing the smallest widths of broad emission lines, i.e. the class of NLS1 sources (Decarli et al. 2008). The black hole mass estimates provided by our method, on the other hand, are scarcely affected by the viewing angle and the geometry of the BLR (§4.2.1).

The Eddington ratios are in the range ℓ =0.04–0.2 (Tab. 3), significantly below the values reported in Y08. This dis-

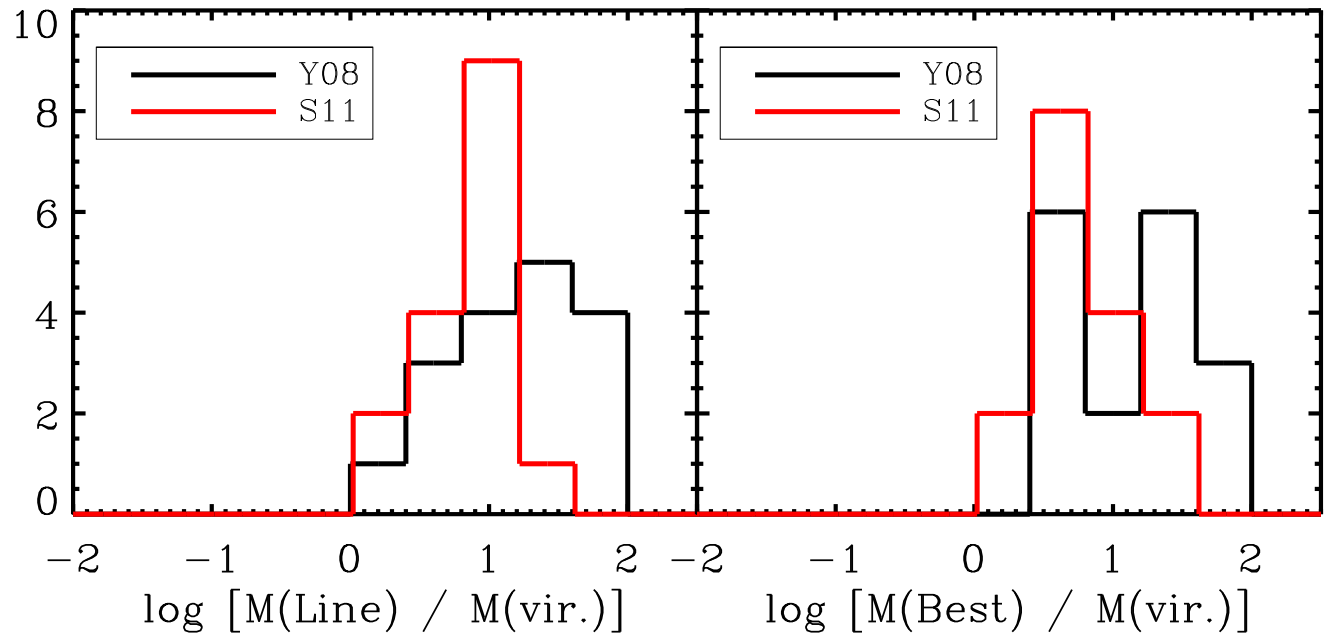

Figure 7. Histogram of our black hole mass estimates to the SE virial ones from the Y08 (left panel) and S11 (right panel) catalogs. Our estimates are greater than SE virial ones by ∼1 dex for Y08 and ∼0.8 for S11 (Eq. 10).

crepancy is due both to our greater black hole mass estimates (a factor ∼6) and to the fact that we used the disk luminosity $L_{\rm d}$ (instead of $L_{\rm bol}$) to compute the Eddington ratio (a factor ∼3.4, Eq. 1 and A16). Hence, our values of Eddington ratio a factor ∼ 20 smaller than SE virial ones on average. With such small values of ℓ the role of radiation pressure in determining the SE virial masses (Marconi et al. 2008; Chiaberge & Marconi 2011) is expected to be small, not sufficient to explain the black hole mass discrepancy.

6.1.1 *The "temperature" argument*

If the assumptions discussed in §4.1 apply, then all the independently estimated black hole masses (even the SE virial ones) should produce an AD spectrum compatible with the observed data. This provides a simple way to compare our results with those reported in Y08 and S11. The black hole mass discrepancy arises because the peak frequencies of the `LINE` and `BEST` AD spectra are significantly lower then the peak frequencies of the Y08 and S11 ones, while the peak luminosities are compatible. If the Y08 and S11 AD models (blue and green lines in Fig. C1) were the correct ones, there must be a physical process able to shift photon to lower frequencies (i.e. to lower "temperatures") in order to account for the observed data. However, such a process cannot exist on a thermodynamic basis, since black body spectra (which build up the AD model) already have the lowest temperature corresponding to a given luminosity and emitting surface. Since the luminosities are the same, the only way to reduce the temperature is to increase the emitting surface, that is by increasing the black hole mass.

7 CONCLUSIONS

In this work we analyzed the relationship between the Big Blue Bump (BBB) observed in the SED of Type 1 AGN and a Shakura & Sunyaev (1973) accretion disk model (AD model). The characteristic disk spectral slope $\alpha_\nu = 1/3$ cannot be directly observed in the AGN SED because of the contributions from other emitting components such as the host galaxy, the torus or (for radio–loud sources) the jet (§2). Once these contributions are taken into account, the observations are compatible with the presence of an emitting component which is well described by an AD model. In particular, the peak of such component can be observed directly in the frequency range $\log(\nu/{\rm Hz}) = 14.8$–$15.5$. By comparing the average Type 1 AGN SED from Richards et al. (2006) with the AD model we calibrate the relations to estimate the total disk luminosity using the continuum line luminosities (at 1350Å, 3000Å and 5100Å) as proxy (§2.1). Furthermore, by using the emission line templates from Francis et al. (1991), we calibrate analogous relations based on the line luminosities of Hβ, Mg II and C IV (§2.2). The latter provide more reliable disk luminosity estimates when the continuum is not dominated by the AD spectrum.

The interpretation of the BBB as being due to the thermal emission from an AD allows to link the AGN observed properties to the properties of the super massive black hole. In particular, the luminosity and frequency at the peak of the AD spectrum uniquely identifies a value for the black hole mass and the accretion rate (§4). However, the direct observation of the peak of the AD spectrum requires broad–band multiwavelength observations. In order to estimate the black hole mass also for sources with a poor observational coverage, we propose a new method which relies only on spectral observations at optical wavelengths. In particular, we constrain the luminosity of the peak by using the line

luminosities. Then we constrain the frequency of the peak by requiring the AD model continuum and slope to reproduce the observed AGN continuum beneath the emission lines (§4.2.1). The maximum uncertainty on our black hole mass estimates is ~ 0.7 dex (on average). This uncertainty is greatly reduced if the disk luminosity can be accurately determined, namely when the peak of the AD spectrum is visible within the frequency range of the data.

We applied our method to the sample of 23 radio–loud Narrow line Seyfert 1 galaxies (RL–NLS1) of Yuan et al. (2008). The method provides reliable black hole mass estimates for 17 sources over 23, if our interpretation of the BBB is correct (§5, 6). The remaining six sources are either dominated by synchrotron radiation from the jet, or do not show "hints" for the presence of an AD–like emitting component. The resulting black hole mass estimates are a factor ~ 6 (on average) greater than the corresponding single epoch virial mass estimates, and the Eddington ratios are a factor ~ 20 below. The discrepancy between our black hole mass estimates and the single epoch virial ones may be due to selection effects occurred in the calibration of the BLR–continuum relation and of the virial factor.

The black hole masses estimated in this paper for the sample of RL–NLS1 are in the interval $\log(M/M_\odot) = 8$–9, and the Eddington ratios are $\ell = 0.04$–0.2. Therefore, very radio–loud NLS1 appear not to be extreme in terms of black hole masses and Eddington ratios. Their black hole masses are similar to those of blazars. We find no evidence for jetted sources with mass below $10^8 M_\odot$.

ACKNOWLEDGMENTS

We acknowledge M. Vestergaard and B.J. Wilkes for having provided the UV iron template. We thank R. Decarli for fruitful discussion.

APPENDIX A: ACCRETION DISK MODEL

A1 Shakura&Sunyaev Accretion Disc (AD)

Here we review the properties of the AD model for a geometrically thin, optically thick accretion disk (Shakura & Sunyaev 1973, hereafter SS73 model) adopted in our analysis of the SED.

The amount of gravitational energy released from each annulus of the disk is given by

$$F(R) = \frac{3}{8\pi}\left(\frac{R}{R_{\rm g}}\right)^{-3}\left[1-\left(\frac{R}{R_{\rm in}}\right)^{-1/2}\right]\frac{\dot{M}c^2}{R_{\rm g}^2} \qquad \text{(A1)}$$

where R is the distance from the black hole, $R_{\rm g} = GM/c^2$ is the gravitational radius of the black hole, $R_{\rm in}$ is the inner radius of the disk. By introducing the adimensional parameters:

$$x = \frac{R}{R_{\rm in}} \qquad \eta = \frac{R_{\rm g}}{2R_{\rm in}} \qquad \text{(A2)}$$

we rewrite the emitted flux as $F(R) = \tilde{F}(x)\,\mathcal{P}$, with

$$\tilde{F}(x) = \frac{3}{\pi}x^{-3}(1-x^{-1/2}) \qquad \mathcal{P} = \eta^3\frac{\dot{M}c^2}{R_{\rm g}^2} \qquad \text{(A3)}$$

where all physical quantities are cast into the $\mathcal{P}$ parameter, while $\tilde{F}(x)$ accounts for dimensionless flux distribution. The total disk luminosity is given by

$$\begin{aligned} L_{\rm d} &= 2\times\int_{R_{\rm in}}^{R_{\rm out}} 2\pi R\ F(R)\ {\rm d}R \\ &= \left[3\int_1^{x_{\rm out}} x^{-2}(1-x^{-1/2})\ {\rm d}x\right]\eta\dot{M}c^2 \end{aligned} \qquad \text{(A4)}$$

where $x_{\rm out} = R_{\rm out}/R_{\rm in}$ is the normalized outer radius of the disk. The quantity in squared parentheses is equal to 1 (provided $R_{\rm out} \gg R_{\rm in}$), therefore the parameter η as defined above is the radiative efficiency of the disk. By assuming $R_{\rm in} = 6R_{\rm g}$ (appropriate for a non–rotating black hole) we obtain $\eta \sim 0.1$.

The maximum amount of energy flux is (by differentiating Eq. A3):

$${\rm MAX}[F(R)] = F(R_{\rm max}) = \frac{64}{\pi}\left(\frac{3}{7}\right)^7\mathcal{P} \qquad \text{(A5)}$$

and it is emitted at a radius $R_{\rm max} = 49/36\ R_{\rm in}$. The assumption of optical thickness implies that each annulus emits radiation as a black body with temperature: $T(R) = [F(R)/\sigma]^{1/4}$. The maximum temperature is therefore (Eq. A5):

$$\frac{T_{\rm max}}{[{\rm K}]} = 3.46\times10^4\left(\frac{\eta}{0.1}\right)^{3/4}\left(\frac{M}{10^9M_\odot}\right)^{-1/2}\left(\frac{\dot{M}}{M_\odot\ {\rm yr}^{-1}}\right)^{1/4} \qquad \text{(A6)}$$

The emitted spectrum is a superposition of black body spectra:

$$\begin{aligned} L_\nu &= 2\times\int_{R_{\rm in}}^{R_{\rm out}} 2\pi\ R\ {\rm d}R\ \pi B[\nu,T(R)] \\ &= 4\pi^2R_{\rm in}^2\mathcal{P}^{3/4}\int_1^{x_{\rm out}} x\ {\rm d}x\ B\left[\frac{\nu}{\mathcal{P}^{1/4}},\left(\frac{\tilde{F}(x)}{\sigma}\right)^{1/4}\right] \end{aligned} \qquad \text{(A7)}$$

where $B[\nu,T(R)]$ is the Planck function. The spectrum profile is completely determined by the dimensionless integral, the only dependences on physical parameters ($\mathcal{P}$) being the characteristic frequency ($\propto \mathcal{P}^{1/4}$) and the overall normalization ($\propto R_{\rm in}^2\mathcal{P}^{3/4}$). The disk spectra are therefore self–similar, and the peak frequency and luminosity scale as:

$$\begin{aligned} \frac{\nu_{\rm p}}{[{\rm Hz}]} &= \mathcal{A}\left(\frac{\eta}{0.1}\right)^{3/4}\left(\frac{M}{10^9M_\odot}\right)^{-1/2}\left(\frac{\dot{M}}{M_\odot\ {\rm yr}^{-1}}\right)^{1/4} \\ \frac{\nu_{\rm p}L_{\nu_{\rm p}}}{[{\rm erg\ s}^{-1}]} &= \mathcal{B}\left(\frac{\eta}{0.1}\right)\left(\frac{\dot{M}}{M_\odot\ {\rm yr}^{-1}}\right) \end{aligned} \qquad \text{(A8)}$$

where $\nu_{\rm p}$ is the frequency of the peak in the νL_ν representation, $\log\mathcal{A} = 15.25$ and $\log\mathcal{B} = 45.36$. By introducing the Eddington ratio $\ell = L_{\rm d}/L_{\rm Edd}$ (with $L_{\rm Edd} = 1.3\times10^{47}(M/10^9M_\odot)$ erg s^{-1}), the previous equations can be rewritten as:

$$\begin{aligned} \frac{\nu_{\rm p}}{[{\rm Hz}]} &= \mathcal{A}\left(\frac{\eta}{0.1}\right)^{1/2}\left(\frac{M}{10^9M_\odot}\right)^{-1/4}\left(\frac{\ell}{0.04}\right)^{1/4} \\ \frac{\nu_{\rm p}L_{\nu_{\rm p}}}{[{\rm erg\ s}^{-1}]} &= \mathcal{B}\left(\frac{M}{10^9M_\odot}\right)\left(\frac{\ell}{0.04}\right) \end{aligned} \qquad \text{(A9)}$$

Notice that, for a given value of η, an estimate of the luminosity and peak frequency allows to determine the physical parameters M and $\dot{M}$.

The spectrum of an AD is shown in Fig. 1 (black solid

line): the superposition of black body spectra, weighted by the surface of emitting annuli produces a "flat" spectrum with slope[8] $\alpha_\nu \sim 1/3$; at highest frequencies, the Wien spectrum from the inner ring dominates, and the overall spectrum decays exponentially.

The self–similarity of AD spectra implies the existence of relations among quantities at the peak frequencies in the L_ν and the νL_ν representations ($\nu_{\rm p'}$ and $\nu_{\rm p}$ respectively), and the disk luminosity $L_{\rm d}$:

$$\frac{\nu_{\rm p}}{\nu_{\rm p'}} = 3.1 \qquad \frac{L_{\nu_{\rm p}}}{L_{\nu_{\rm p'}}} = 0.66 \qquad \frac{\nu_{\rm p} L_{\nu_{\rm p}}}{L_{\rm d}} = 0.5 \quad \text{(A10)}$$

Also, note that the peak luminosity $\nu_{\rm p} L_{\nu_{\rm p}}$ is independent from the actual value of $R_{\rm out}$, as long as $R_{\rm out} \gtrsim 10\, R_{\rm in}$. The relation between the maximum temperature in the disk and the color temperature of the AD spectrum (i.e. the black body temperature associated to the peak frequency $\nu_{\rm p'}$) is $T_{\rm max} = 3.5\ T_{\rm col}$.

A2 Peak shift

The physical parameters η, M and $\dot{M}$ uniquely identify the frequency and luminosity of the spectral peak (Eq. A8 or A9). Variations of one or more of these parameters will shift the peak along specific directions, whose slope in a $\log \nu L_\nu$ vs. $\log \nu$ plot is given by:

$$\alpha = \frac{{\rm d} \log \nu_{\rm p} L_{\nu_{\rm p}}}{{\rm d} \log \nu_{\rm p}} \quad \text{(A11)}$$

Here is a list of peak shift relations used in this work:

(i) vertical shift ($\alpha = \infty$): variations in M, $\dot{M}$ with constant $\dot{M}/M^2$ ratio (fixed η);
(ii) horizontal shift ($\alpha = 0$): variations in M with constant $\dot{M}$ (fixed η);
(iii) $\alpha = 4$: variations in $\dot{M}$, with constant M (fixed η);
(iv) $\alpha = -4$: variations in M and $\dot{M}$, with constant $\ell \propto \dot{M}/M$ (fixed η);
(v) no shift: variations in all parameters, with constant $\eta\dot{M}$ and η/M.

In particular, case (v) is used in §6.1 to show that if the actual radiative efficiency η is greater than hypothesized in §4.1, then our black hole mass estimate is a lower limit. The physical interpretation of case (v) is depicted in Fig. A1. By following the black hole mass estimation method outlined §4.2.1 we identify an AD model (black line) in agreement with observed data (brown line): the peak lies at the "ceiling" luminosity level determined by broad line luminosities (Eq. 7) and the AD spectrum is in agreement with the observed continuum. This model relies on the assumption of radiative efficiency $\eta \sim 0.1$. However, the actual value of efficiency may be different. By increasing the η parameter (i.e. decreasing the inner radius of the disk $R_{\rm in}$) the peak shifts to higher frequencies and luminosities as radiation comes from the inner, hotter radii (blue line). This new model would no longer be in agreement with the "ceiling" luminosity argument, therefore we must decrease the accretion rate (green line), leaving M and η unchanged. Still, the obtained spectrum is not in agreement with the observed continuum, therefore we must decrease the "temperature" of the spectrum (§6.1.1), by increasing M (red line). The final AD model is again in agreement with observed data, but has higher values of η and M (and a lower value of $\dot{M}$).

[8] The slope $\alpha_\nu = 1/3$ is achieved only for $R_{\rm out} \to \infty$. For a finite value of the outer radius of the disk, such as the one used in this work $R_{\rm out} = 2 \times 10^3 R_{\rm g}$, a more realistic value for the slope is $\alpha_\nu \sim 1/4$.

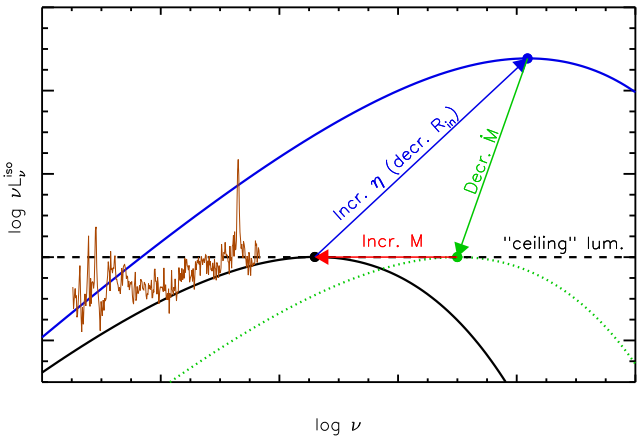

Figure A1. The black hole mass estimate provided by the AD modeling procedures (§4) show a linear dependence on the assumed value of the radiative efficiency: $M \propto \eta$ (case (v) in §A2). The physical interpretation of this dependence is shown in the figure: the AD model (black line) identified with either the `LINE` or `BEST` procedure is in agreement with observed data (brown line). In particular the peak lies at the "ceiling" luminosity level determined by broad line luminosities (Eq. 7) and the AD spectrum is in agreement with the AGN continuum. By increasing the η parameter (i.e. decreasing the inner radius of the disk $R_{\rm in}$) the peak shifts to higher frequencies and luminosities as radiation comes from the inner, hotter radii (blue line). This new model would no longer be in agreement with the "ceiling" luminosity argument, therefore we must decrease the accretion rate (green line), leaving M and η unchanged. Still, the obtained spectrum is not in agreement with the observed continuum, therefore we must decrease the "temperature" of the spectrum (§6.1.1), by increasing M (red line). The final AD model is again in agreement with observed data, but has higher values of η and M (and a lower value of $\dot{M}$).

A3 Observational properties

The emission from the whole (geometrically thin) disk is anisotropic since the observed flux is proportional to the projected area seen by the observer, i.e. $F_\nu \propto \cos\theta$, where θ is the viewing angle. By requiring $\oint_{\rm Sph.} F_\nu D_{\rm L}^2 d\Omega = L_\nu$ we obtain:

$$L_\nu = \frac{2\pi D_{\rm L}^2 F_{\nu_o}}{(1+z)\cos\theta} \quad \text{(A12)}$$

where $D_{\rm L}$ is the luminosity distance, $\nu_o = \nu/(1+z)$ is the observed frequency and F_{ν_o} is the observed flux density. Note that the luminosity–flux relation for a thin disk is different from the isotropic case, in particular the relation between the "isotropic equivalent" luminosity and the real luminos-

ity is:

$$L_\nu^{\rm iso} = 2\cos\theta L_\nu \quad \text{(A13)}$$

The observed flux is therefore (from Eq. A7, A12):

$$F_{\nu_o} = \frac{4\pi h\nu_o^3}{c^2 D_{\rm L}^2}(1+z)\cos\theta \int_{R_{\rm in}}^{R_{\rm out}} \frac{R\ {\rm d}R}{\exp\left(h\nu/kT\right)-1} \quad \text{(A14)}$$

The model for the observed spectrum has four parameters: M, $\dot{M}$, $R_{\rm in}$ and $\cos\theta$ (the value of $R_{\rm out}$ is not important here) which are related to quantities in Eq. A14 through the temperature distribution given in Eq. A1. Not all parameter can be constrained observationally, since the viewing angle is degenerate with both $\dot{M}$ and M. Hence we are forced to make a simplifying assumption about the inclination angle: since we are interested in Type 1 AGN, we assume that the viewing angle is in the range 0–45 deg, i.e. the aperture of the obscuring torus. If observed at a greater angle, the source would likely be classified as a Type 2 AGN. The average value of $\cos\theta$ (where θ is measured from the disk normal) is:

$$\langle\cos\theta\rangle = \frac{1+\cos\theta_{\rm max}}{2} \quad \text{(A15)}$$

By setting $\theta_{\rm max}$=45 deg we obtain $\langle\cos\theta\rangle$=0.854, corresponding to an average viewing angle of ∼30 deg. With this assumption Eq. A13 reads:

$$L_\nu^{\rm iso} \sim 1.7\ L_\nu \quad \text{(A16)}$$

A4 General relativistic corrections

The general relativistic model for the accretion disk is described in Novikov & Thorne (1973) and Page & Thorne (1974). The differences with respect to the AD model influencing the observational appearance of the spectrum are:

(i) the innermost stable circular orbit (isco) depends on the spin parameter $a = Jc/GM^2$. For a non–rotating black hole ($a = 0$) $R_{\rm isco} = 6R_{\rm g}$. The maximum spin of an accreting black hole is $a = 0.998$ (Thorne 1974), with $R_{\rm isco} = 1.24R_{\rm g}$. The binding energy of a particle at $R_{\rm isco}$ in units of the particle rest–mass is (e.g. Cunningham 1975):

$$\eta_{\rm gr} = 1 - \sqrt{1 - \frac{2}{3}\frac{R_{\rm g}}{R_{\rm isco}}} \quad \text{(A17)}$$

i.e. $\eta_{\rm gr}(a=0) \sim 0.06$ and $\eta_{\rm gr}(a=0.998) \sim 0.32$. This is expected to be the maximum possible value for the radiative efficiency (compare Eq. A3).

(ii) the different radial distribution of energy flux (Page & Thorne 1974; Zhang et al. 1997) with respect to Eq. A1. The resulting spectrum is still the superposition of black body spectra;

(iii) the spectrum received by distant observers is influenced by gravitational redshift, Doppler boost and gravitational bending of light (Cunningham 1975).

Li et al. (2005) have developed a package to synthesize the observed spectrum for an optically thick, geometrically thin accretion disk around a Kerr black hole, taking into account all these effects. The code is available as the model `KERRBB` within the X-ray data reduction package XSPEC (Arnaud 1996). In the following we will compare the spectral profiles of both the "classical" and "relativistic" models, and show that the differences are negligible for the purpose of our work.

We compute the accretion disk flux, as received by an observer at a given distance, using both the the SS73 and `KERRBB` models. The black hole mass, accretion rate and distance of the observer will be kept fixed for all the considered models.

We consider five SS73 AD models, by varying the inner radius of the disk $R_{\rm in}$. The values of $R_{\rm in}$ has been chosen in order to reduce the discrepancies between SS73 and `KERRBB` models (see below). We take the model with $R_{\rm in} = 6R_{\rm g}$ as a reference spectrum, and normalize all other SS73 spectra by the luminosity of its peak ($\nu_{\rm p}F_{\nu_{\rm p,ref}}$). These spectra are shown with solid lines in Fig. A2. Note that the only dependence on the viewing angle θ for the SS73 model is due to the projected area seen by the observer, i.e. to a factor $\cos\theta$. By plotting spectra normalized by $\cos\theta$ we completely remove this dependence.

Then we consider five groups of `KERRBB` models, by varying the spin of the black hole: $a = -1, 0, 0.4, 0.7$ and 0.998. These values span the entire range of allowed values for the spin of an accreting black hole (Thorne 1974). For each value of the spin, we consider three different viewing angles: $\theta = 0^\circ, 30^\circ$ and 45°. All spectra are normalized by the luminosity $\nu_{\rm p}F_{\nu_{\rm p,ref}}$ of the reference SS73 model discussed above, and by $\cos\theta$. These spectra are shown with dotted, dashed and dot–dashed lines in Fig. A2. Note that the `KERRBB` models show a residual dependence on the viewing angle, due to light bending and Doppler boosting.

The values of $R_{\rm in}$ has been chosen in order to allow the SS73 spectra to resemble as close as possible the `KERRBB` spectra, at given values of spin. The profile of the normalized spectra are indeed very similar (spectra of the same color), the differences being at most ±0.1 dex for the highest value of spin ($a = 0.998$). The (empirical) relation between the $R_{\rm in}$ in the SS73 model and the radiative efficiency of the corresponding `KERRBB` model is:

$$\frac{R_{\rm in}}{R_{\rm g}} = \frac{1}{2\eta_{\rm gr}} + 1.25 \quad \text{(A18)}$$

where $\eta_{\rm gr}$ is given by Eq. A17.

From the observational point of view, the SS73 AD model with $R_{\rm in} = 6R_{\rm g}$ (used throughout this work) mimics the `KERRBB` model with spin $a \sim 0.7$ ($\eta_{\rm gr} \sim 0.1$), as long as frequencies below the peak are concerned. Therefore, the results of our work are not influenced by having neglected the general relativistic corrections in modeling the accretion disk spectrum.

REFERENCES

Abazajian K. N., et al., 2009, ApJS, 182, 543
Abdo A. A., et al., 2009a, ApJ, 699, 976
Abdo A. A., et al., 2009b, ApJ, 707, 727
Abdo A. A., et al., 2009c, ApJ, 707, L142
Arnaud K. A., 1996, in Jacoby G. H., Barnes J., eds, Astronomical Data Analysis Software and Systems V Vol. 101 of Astronomical Society of the Pacific Conference Series, XSPEC: The First Ten Years. p. 17
Assef R. J., Frank S., Grier C. J., Kochanek C. S., Denney K. D., Peterson B. M., 2012, ApJ, 753, L2

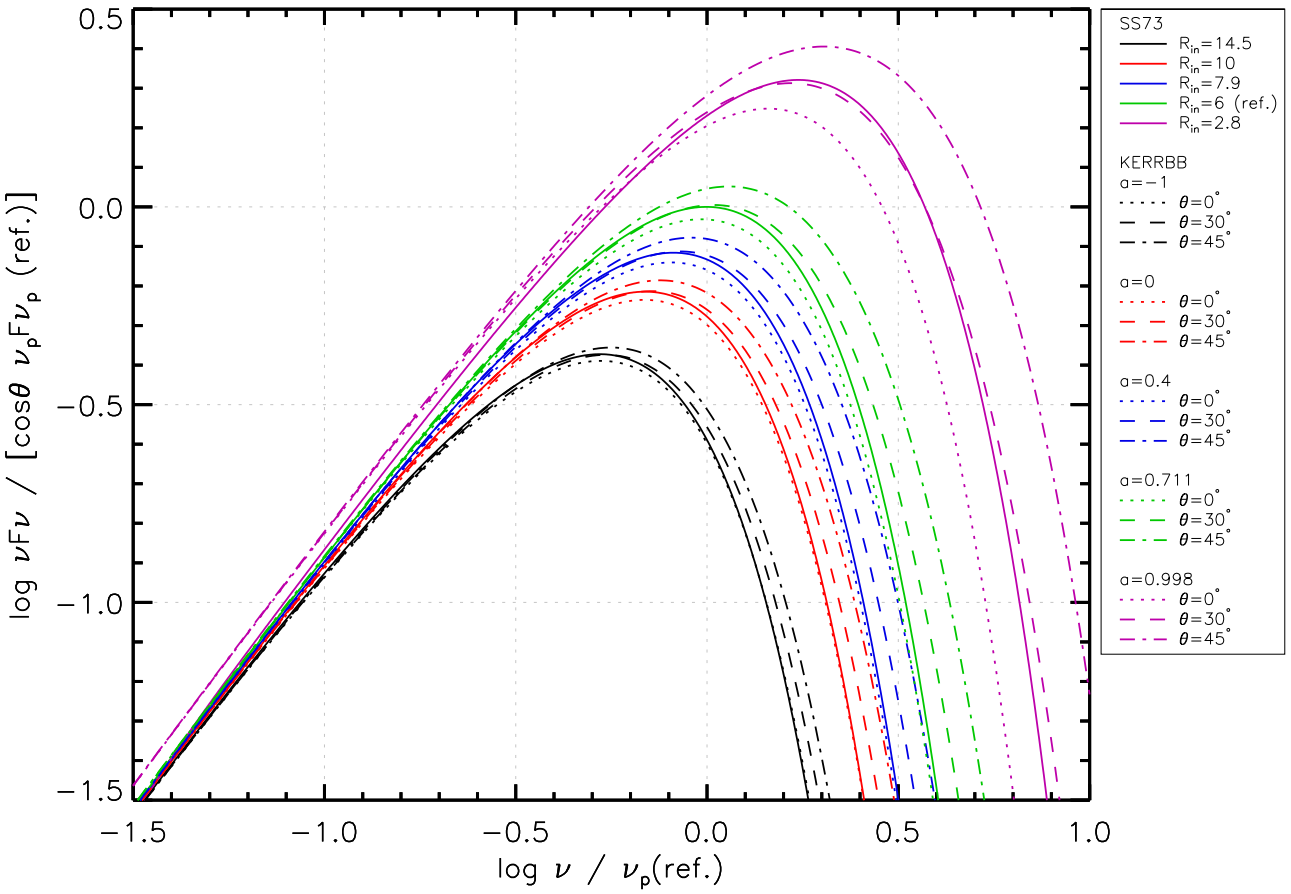

Figure A2. Comparison between the SS73 (Shakura & Sunyaev 1973, solid lines) and the `KERRBB` (Li et al. 2005, dotted, dashed and dot–dashed lines) accretion disk spectra. The SS73 spectrum with $R_{\rm in} = 6\,R_{\rm g}$ is used as a reference spectrum: all other spectra are normalized by its peak luminosity. We consider three viewing angles $\theta = 0°, 30°$ and $45°$, and normalize all spectra by $\cos\theta$. This completely removes the dependence of the SS73 on the viewing angle. The `KERRBB` show a residual dependence on the viewing angle (dotted, dashed and dot–dashed lines). The colors identify a value for the inner radius of the SS73 model (respectively $R_{\rm in}/R_{\rm g} = 14.5, 10, 7.9, 6$ and 2.8) and for the black hole spin of the `KERRBB` model (respectively $a = -1, 0, 0.4, 0.7, 0.998$). The inner radii for the SS73 models have been chosen in order to allow the SS73 spectra to resemble as close as possible the `KERRBB` spectra, at given values of the spin. The resulting empirical relation between $R_{\rm in}$ and the radiative efficiency of the `KERRBB` model (Eq. A17) is given in Eq. A18.

Bentz M. C., Peterson B. M., Netzer H., Pogge R. W., Vestergaard M., 2009, ApJ, 697, 160

Bonning E. W., Cheng L., Shields G. A., Salviander S., Gebhardt K., 2007, ApJ, 659, 211

Calderone G., Foschini L., Ghisellini G., Colpi M., Maraschi L., Tavecchio F., Decarli R., Tagliaferri G., 2011, MNRAS, 413, 2365

Calderone G., Ghisellini G., Colpi M., Dotti M., 2012, MNRAS, 424, 3081

Calderone G., Sbarrato T., Ghisellini G., 2012, MNRAS, p. L482

Cardelli J. A., Clayton G. C., Mathis J. S., 1989, ApJ, 345, 245

Celotti A., Padovani P., Ghisellini G., 1997, MNRAS, 286, 415

Chiaberge M., Marconi A., 2011, MNRAS, 416, 917

Croom S. M., 2011, ApJ, 736, 161

Cunningham C. T., 1975, ApJ, 202, 788

Davis S. W., Laor A., 2011, ApJ, 728, 98

Davis S. W., Woo J.-H., Blaes O. M., 2007, ApJ, 668, 682

Decarli R., Dotti M., Fontana M., Haardt F., 2008, MNRAS, 386, L15

Decarli R., Dotti M., Treves A., 2011, MNRAS, 413, 39

Elvis M., et al., 1994, ApJS, 95, 1

Fabian A. C., Miniutti G., 2005, ArXiv Astrophysics e-prints

Ferrarese L., Ford H., 2005, Space Sci. Rev., 116, 523

Foschini L., 2011 in Proceedings of "Narrow-Line Seyfert 1 Galaxies and their Place in the Universe". `(arXiv:1105.0772)`

Foschini L., et al., 2011, MNRAS, 413, 1671

Franceschini A., Vercellone S., Fabian A. C., 1998, MNRAS, 297, 817

Francis P. J., Hewett P. C., Foltz C. B., Chaffee F. H., Weymann R. J., Morris S. L., 1991, ApJ, 373, 465

Ghisellini G., Tavecchio F., Foschini L., Ghirlanda G., Maraschi L., Celotti A., 2010, MNRAS, 402, 497

Grupe D., Komossa S., Leighly K. M., Page K. L., 2010,

ApJS, 187, 64
Grupe D., Mathur S., 2004, ApJ, 606, L41
Kellermann K., Sramek R., Schmidt M., Shaffer D. B., Green R., 1989, AJ, 98, 1195
Kishimoto M., Antonucci R., Blaes O., Lawrence A., Boisson C., Albrecht M., Leipski C., 2008, Nature, 454, 492
Koratkar A., Blaes O., 1999, PASP, 111, 1
Krolik J. H., 2001, ApJ, 551, 72
Laor A., 2000, ApJ, 543, L111
Laor A., Davis S., 2011a, arXiv:1110.0653
Laor A., Davis S. W., 2011b, MNRAS, 417, 681
Li L.-X., Zimmerman E. R., Narayan R., McClintock J. E., 2005, ApJS, 157, 335
Malkan M. A., 1983, ApJ, 268, 582
Malkan M. A., Sargent W. L. W., 1982, ApJ, 254, 22
Mannucci F., Basile F., Poggianti B. M., Cimatti A., Daddi E., Pozzetti L., Vanzi L., 2001, MNRAS, 326, 745
Marconi A., Axon D. J., Maiolino R., Nagao T., Pastorini G., Pietrini P., Robinson A., Torricelli G., 2008, ApJ, 678, 693
Martin D. C., et al., 2005, ApJ, 619, L1
Mathur S., Grupe D., 2005, ApJ, 633, 688
Nandra K., Pounds K. A., 1994, MNRAS, 268, 405
Neugebauer G., Oke J. B., Becklin E. E., Matthews K., 1979, ApJ, 230, 79
Novikov I. D., Thorne K. S., 1973, in Dewitt C., Dewitt B. S., eds, Black Holes (Les Astres Occlus) Astrophysics of black holes.. pp 343–450
O'Donnell J. E., 1994, ApJ, 422, 158
Onken C. A., Ferrarese L., Merritt D., Peterson B. M., Pogge R. W., Vestergaard M., Wandel A., 2004, ApJ, 615, 645
Osterbrock D. E., Pogge R. W., 1985, ApJ, 297, 166
Page D. N., Thorne K. S., 1974, ApJ, 191, 499
Park D., Woo J.-H., Treu T., Barth A. J., Bentz M. C., Bennert V. N., Canalizo G., Filippenko A. V., Gates E., Greene J. E., Malkan M. A., Walsh J., 2012, ApJ, 747, 30
Peterson B. M., 1993, PASP, 105, 247
Peterson B. M., 2011, arXiv:1109.4181
Peterson B. M., et al., 2004, ApJ, 613, 682
Pogge R. W., 2000, New Astronomy Review, 44, 381
Pounds K. A., Warwick R. S., Culhane J. L., de Korte P. A. J., 1986, MNRAS, 218, 685
Raimundo S. I., Fabian A. C., Vasudevan R. V., Gandhi P., Wu J., 2012, MNRAS, 419, 2529
Richards G. T., et al., 2006, ApJS, 166, 470
Sanders D. B., Phinney E. S., Neugebauer G., Soifer B. T., Matthews K., 1989, ApJ, 347, 29
Sbarrato T., Ghisellini G., Nardini M., Tagliaferri G., Foschini L., Ghirlanda G., Tavecchio F., Greiner J., Rau A., Gehrels N., 2012, MNRAS, 426, L91
Schlegel D. J., Finkbeiner D. P., Davis M., 1998, ApJ, 500, 525
Shakura N. I., Sunyaev R. A., 1973, A&A, 24, 337
Shen Y., et al., 2011, ApJS, 194, 45
Shields G. A., 1978, Nature, 272, 706
Sun W.-H., Malkan M. A., 1989, ApJ, 346, 68
Telfer R. C., Zheng W., Kriss G. A., Davidsen A. F., 2002, ApJ, 565, 773
Thorne K. S., 1974, ApJ, 191, 507
Vanden Berk D. E., et al., 2001, AJ, 122, 549
Véron-Cetty M.-P., Joly M., Véron P., 2004, A&A, 417, 515
Vestergaard M., Peterson B. M., 2006, ApJ, 641, 689
Vestergaard M., Wilkes B. J., 2001, ApJS, 134, 1
Walter R., Fink H. H., 1993, A&A, 274, 105
Wills B. J., Netzer H., Wills D., 1985, ApJ, 288, 94
Woo J.-H., Urry C. M., 2002, ApJ, 581, L5
Wright E. L., et al., 2010, AJ, 140, 1868
York D. G., et al., 2000, AJ, 120, 1579
Yuan W., Zhou H. Y., Komossa S., Dong X. B., Wang T. G., Lu H. L., Bai J. M., 2008, ApJ, 685, 801
Zhang S. N., Cui W., Chen W., 1997, ApJ, 482, L155
Zheng W., et al., 1995, ApJ, 444, 632
Zhou H., Wang T., Yuan W., Lu H., Dong X., Wang J., Lu Y., 2006, ApJS, 166, 128

APPENDIX B: FIGURES: SPECTRAL FITTING

This appendix is a collection of the figures related to the spectral fitting procedure discussed in §3.1. On the left panels we show the whole rest frame wavelength range, while on the right panels we show a detailed view on the Hβ, [O III] and Mg II regions. The SDSS data and associated uncertainties are shown with black squares and grey lines respectively. Also shown are the fitting models (red lines), as well as the individual components: the AGN continuum (black), the galaxy template (cyan), the jet component (as extrapolated from WISE photometry, purple), the iron templates (orange), the broad (blue) and narrow (green) emission lines, and the additional emission lines (grey). In lower part of left panels we show the residuals in units of data uncertainties. The red lines show the cumulative $\chi^2_{\rm red}$ (values on right axis).

APPENDIX C: FIGURES: BLACK HOLE MASS ESTIMATION

This appendix is a collection of the figures related to the black hole mass estimation procedures described in §4, adopting the same notation as in Fig. 4.

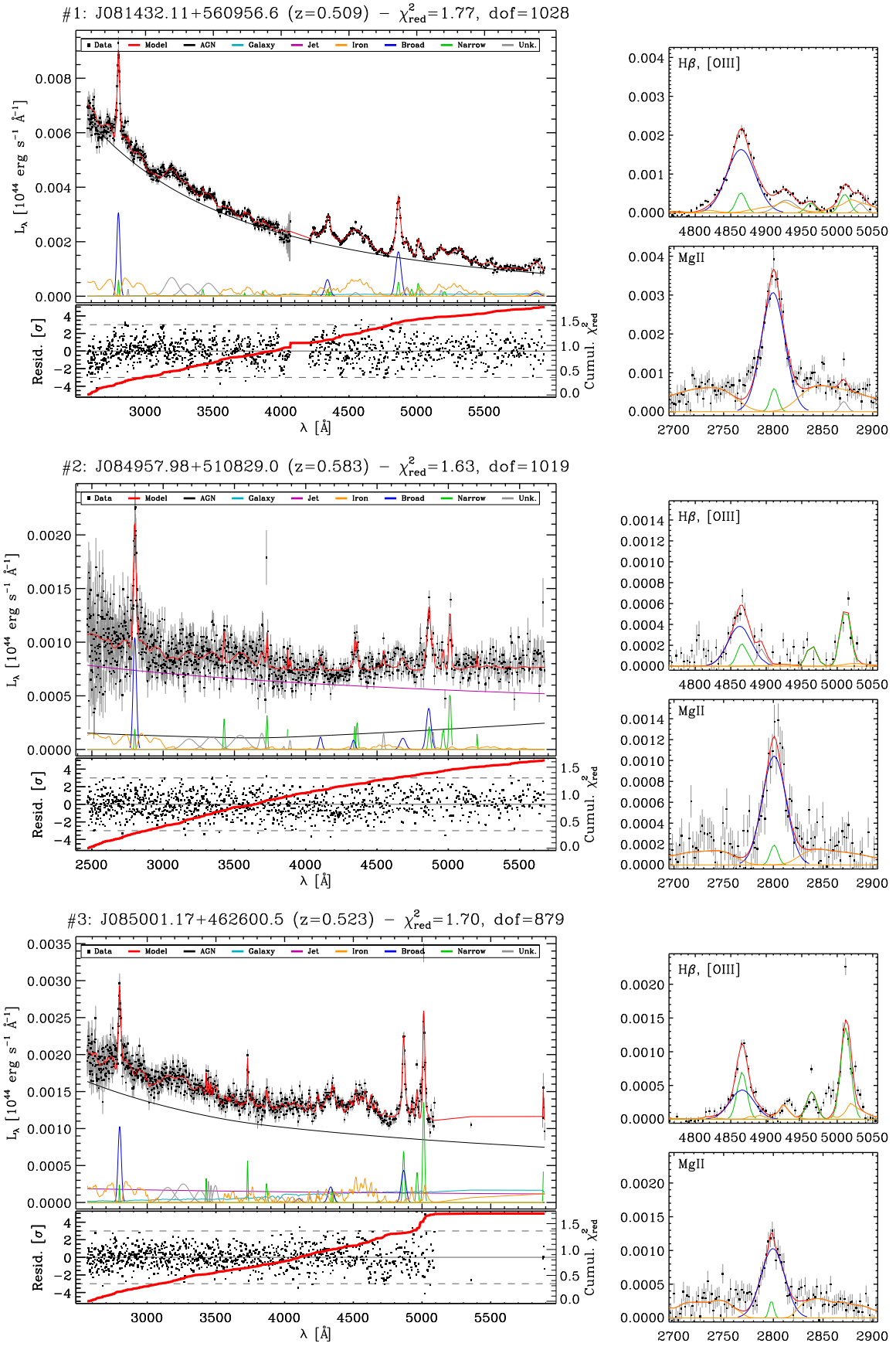

Figure B1. Results of the spectral fitting procedure (§3.1, App. B).

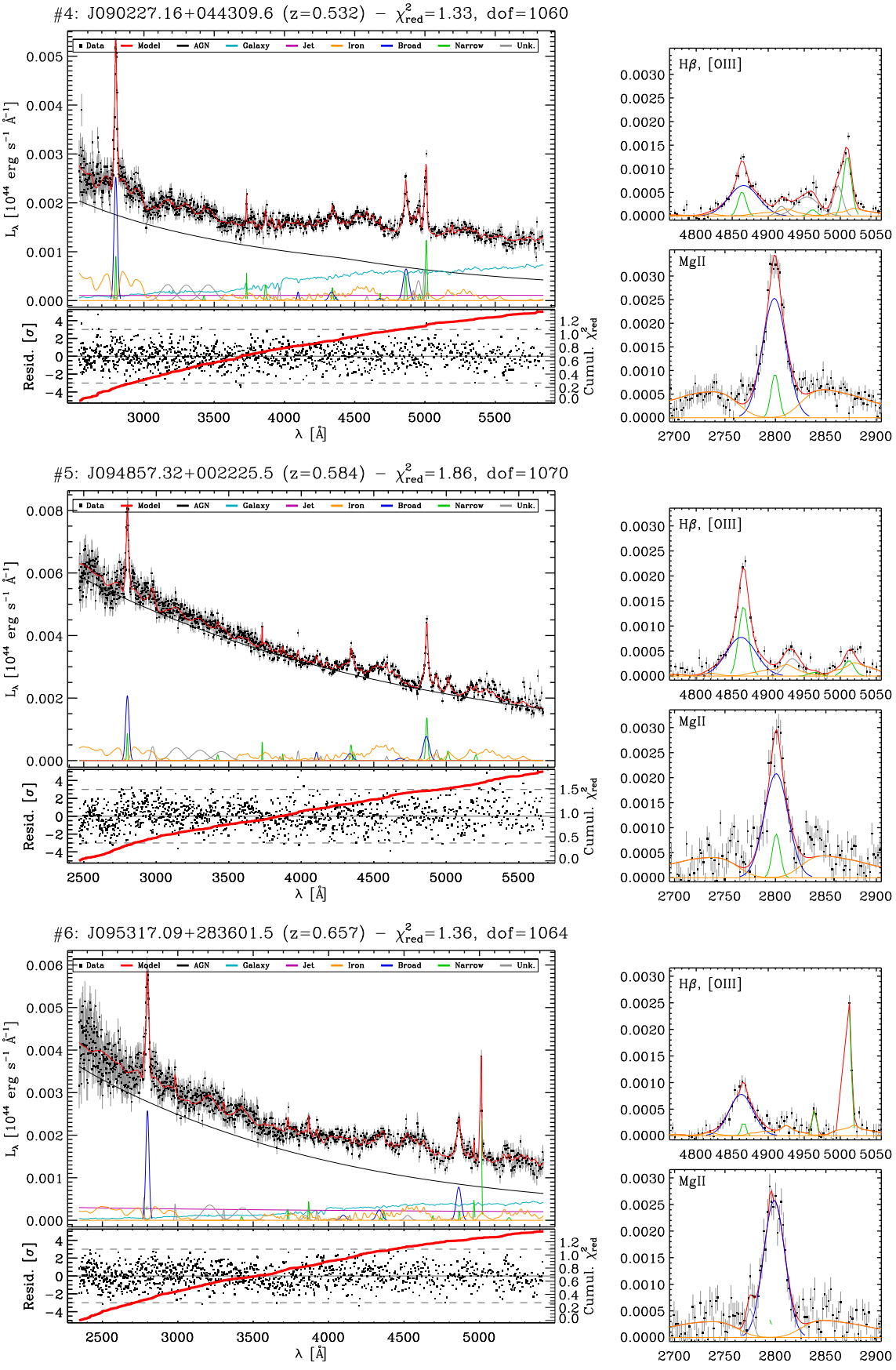

Figure B1. (continued)

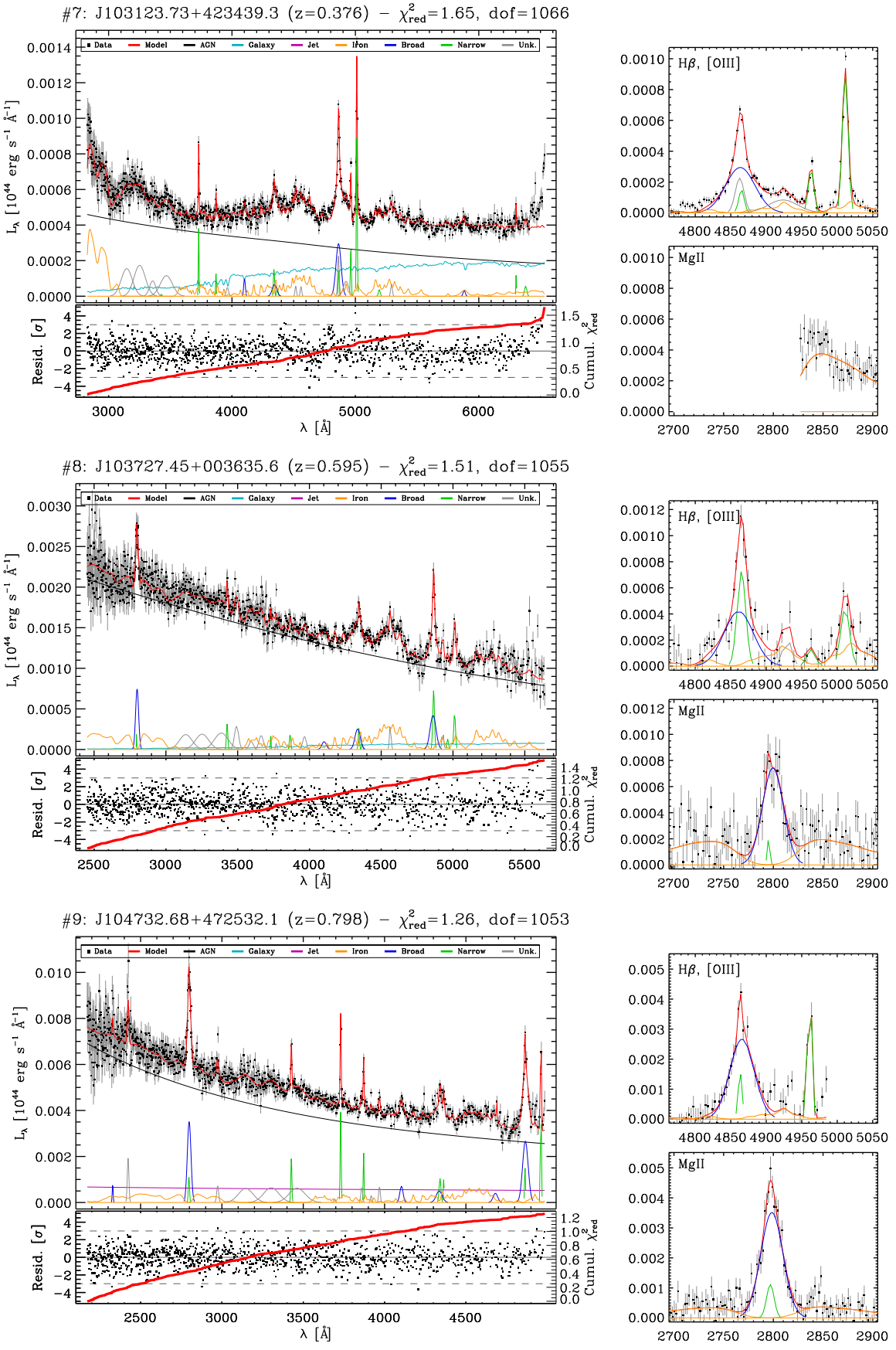

Figure B1. (continued)

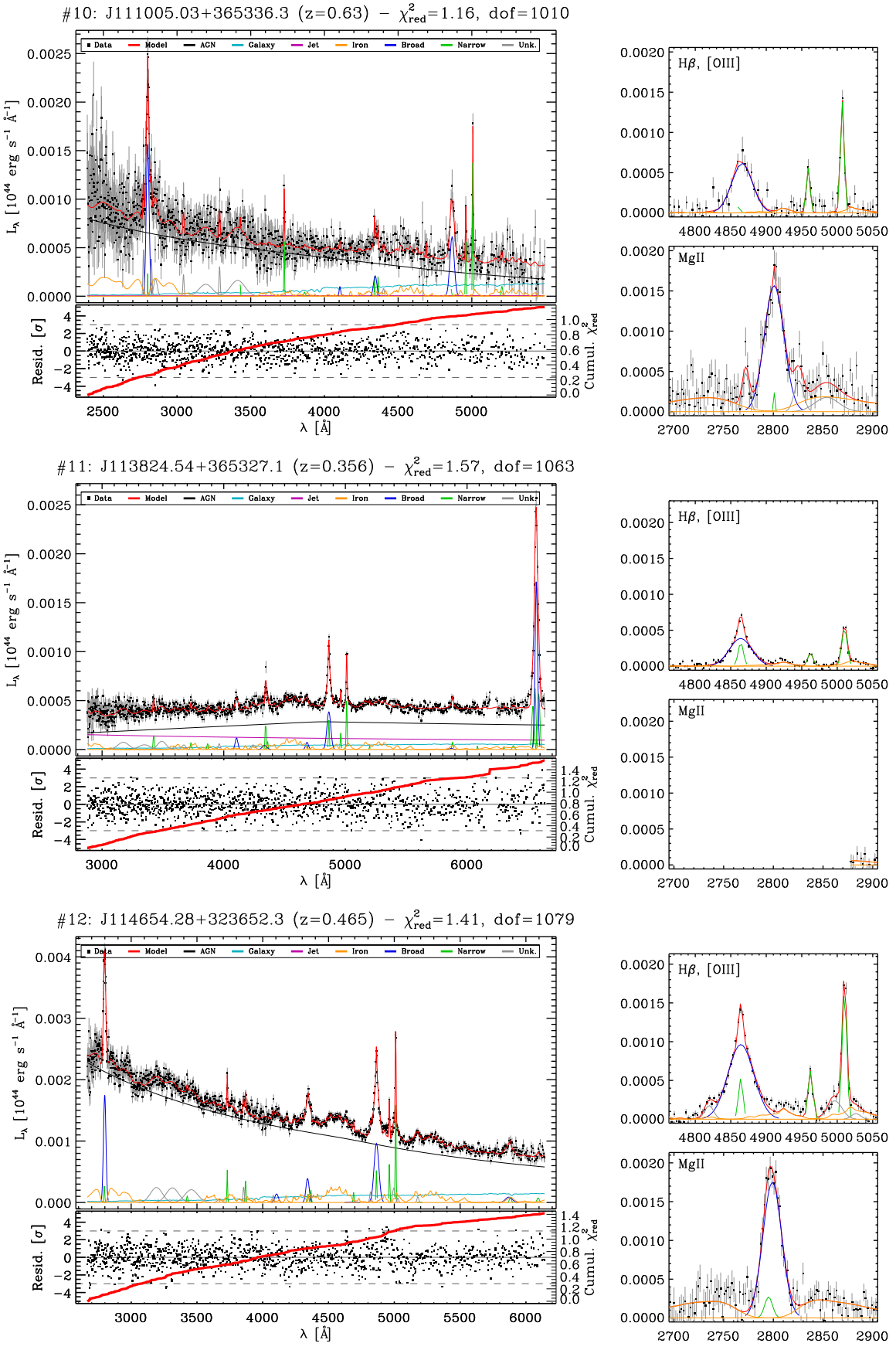

Figure B1. (continued)

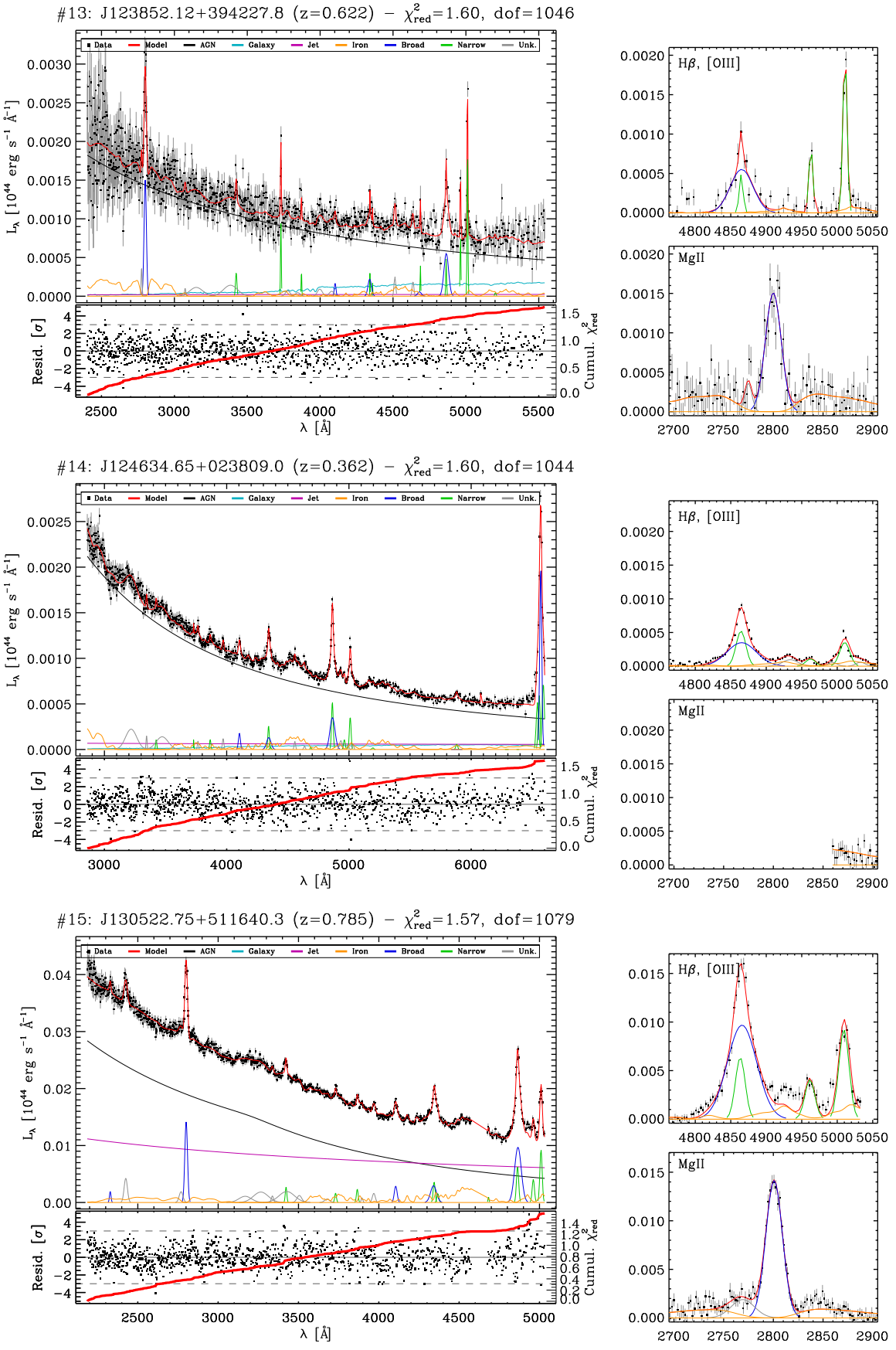

Figure B1. (continued)

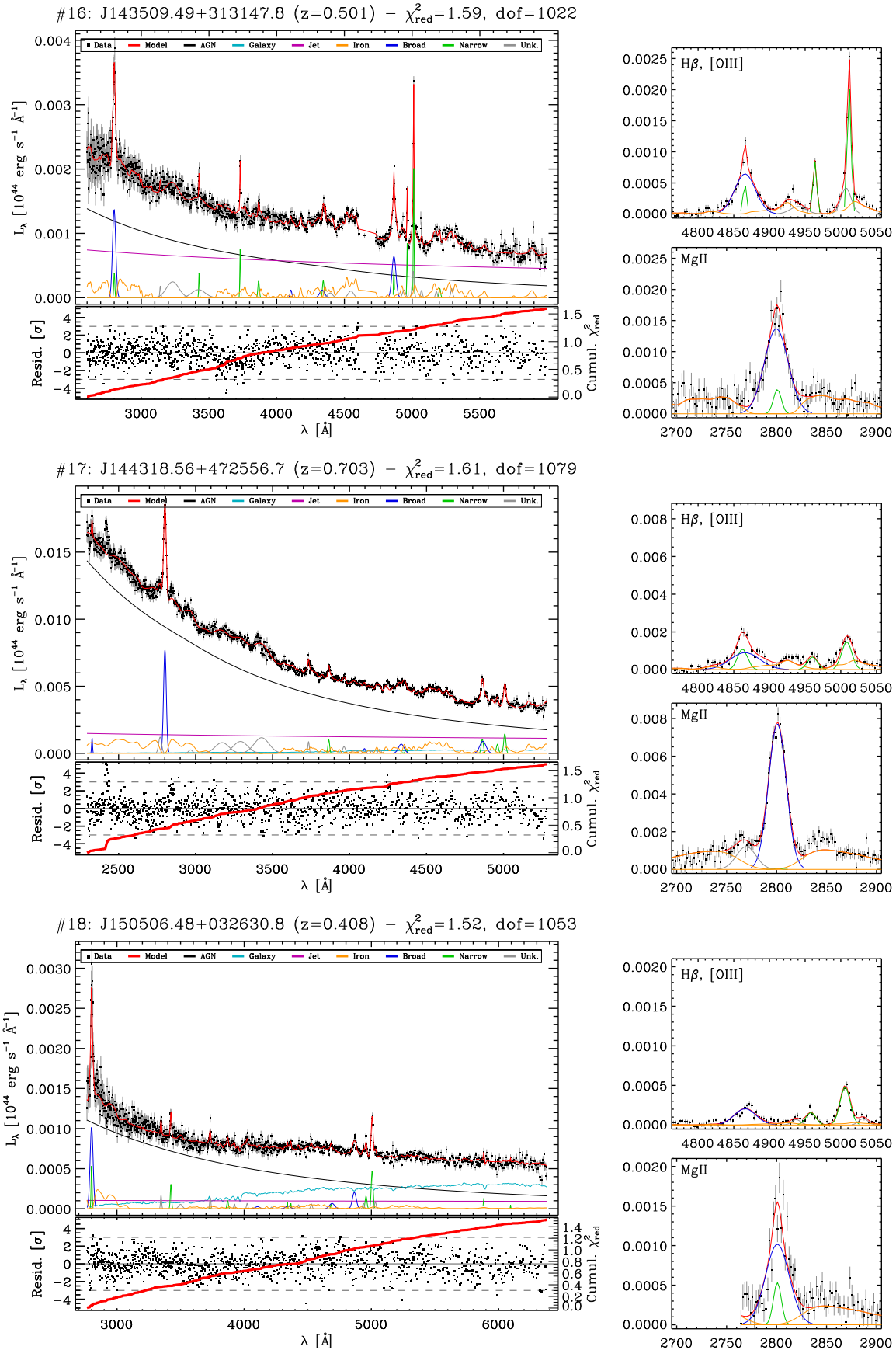

Figure B1. (continued)

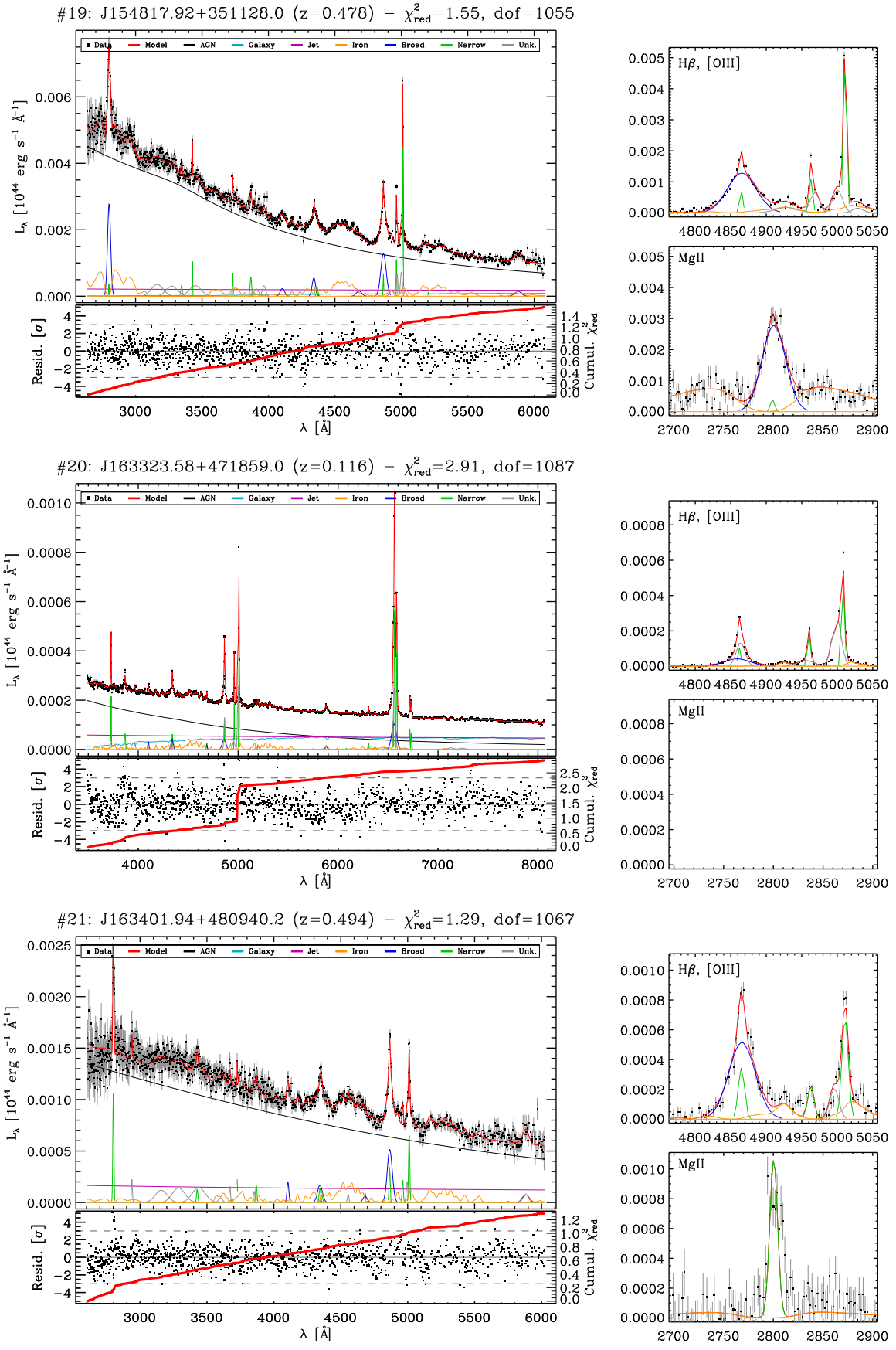

Figure B1. (continued)

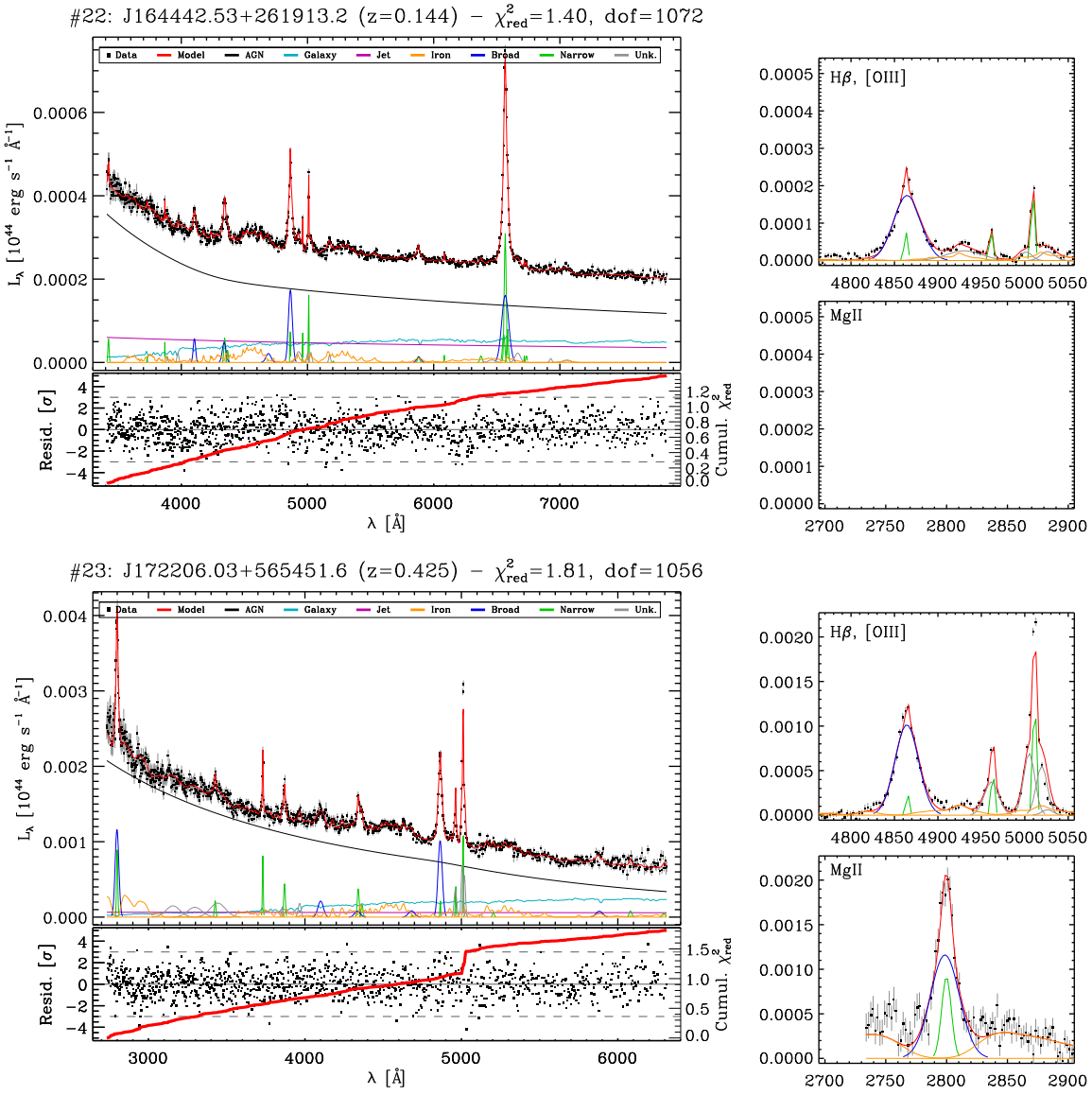

Figure B1. (continued)

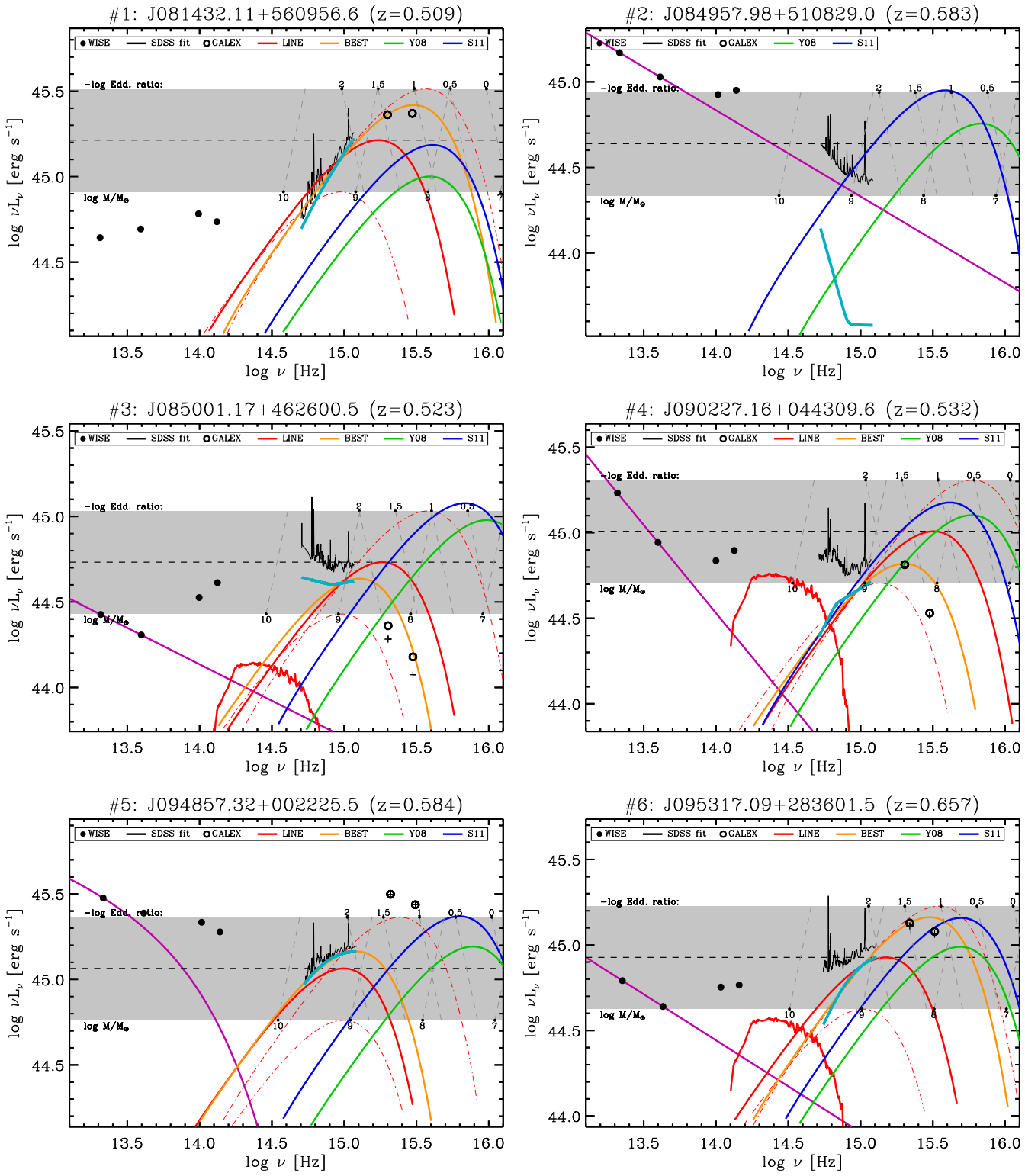

Figure C1. Results of the black hole mass estimation procedures (§4, App. C). Notation is the same as in Fig. 4.

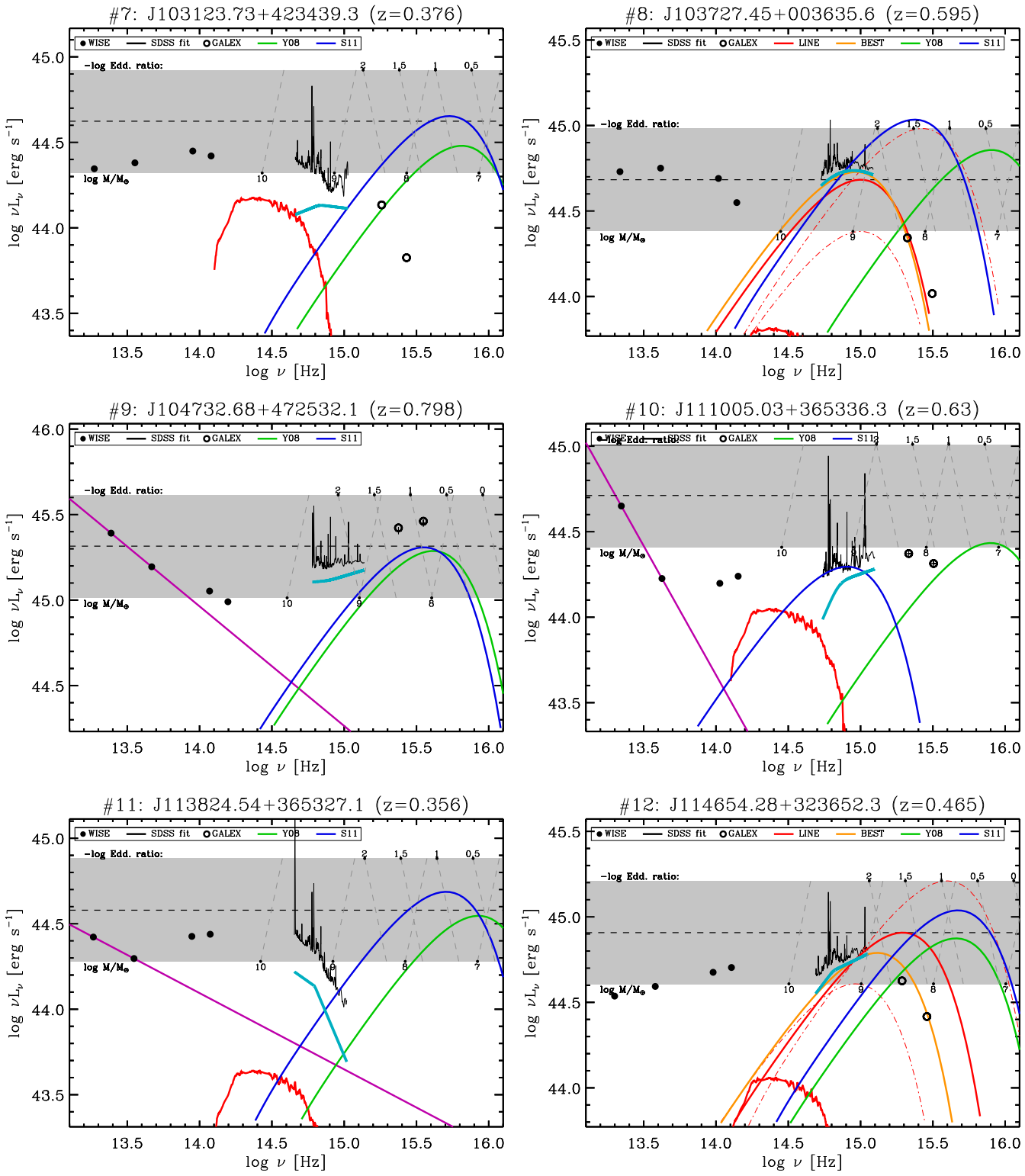

Figure C1. (continued)

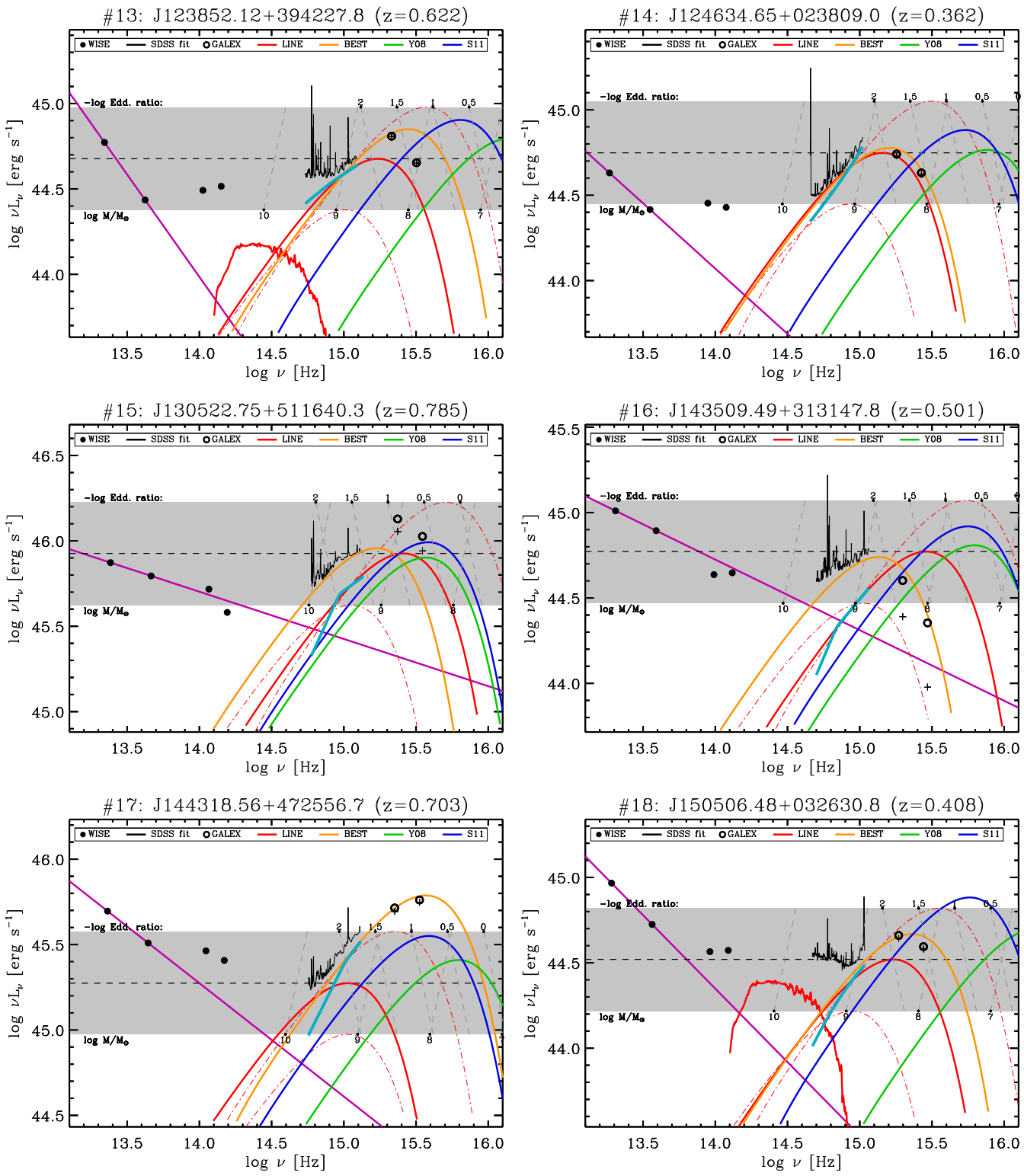

Figure C1. (continued)

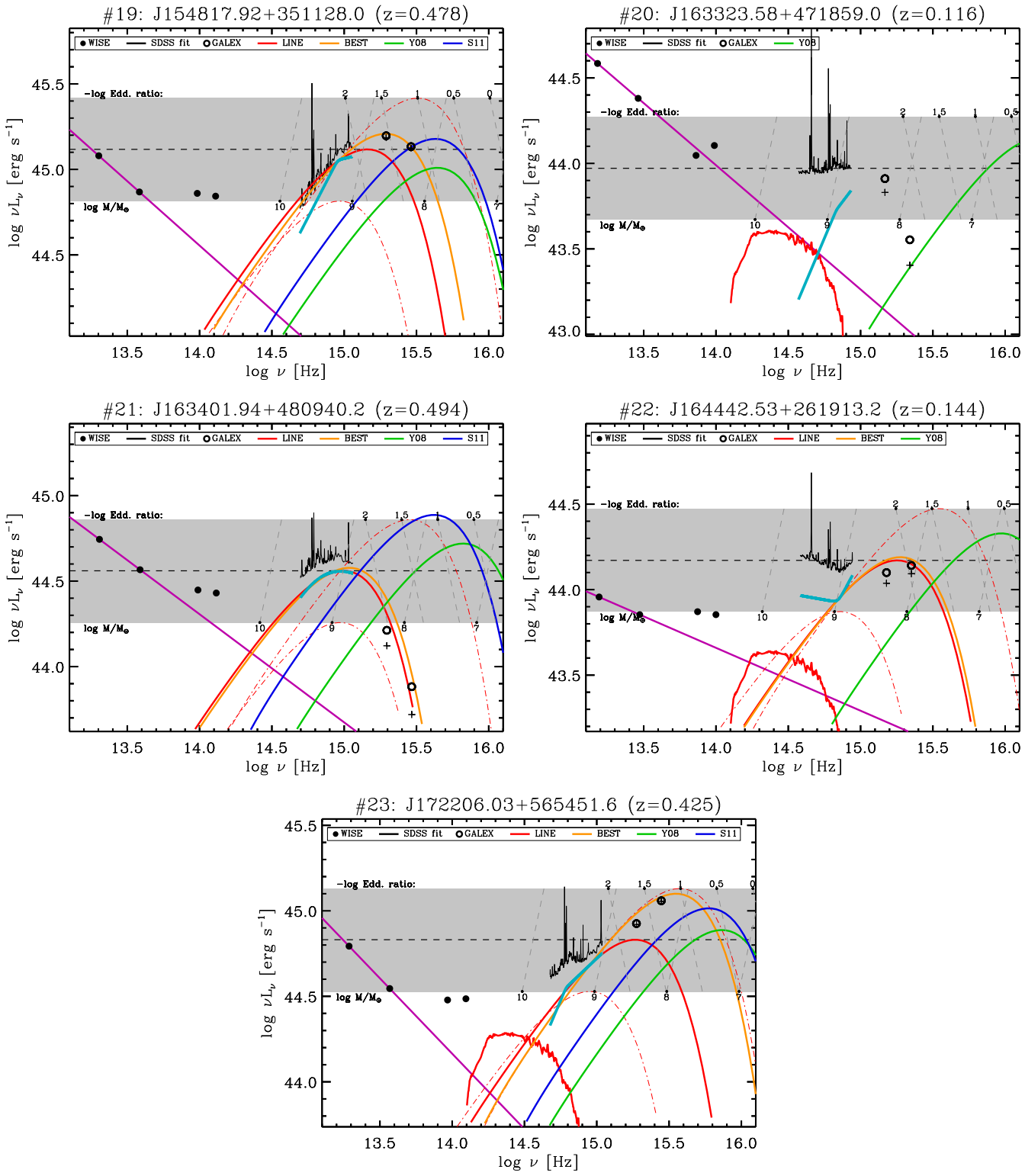

Figure C1. (continued)